

## Article

# Application of Dirichlet Process and Support Vector Machine Techniques for Mapping Alteration Zones Associated with Porphyry Copper Deposit Using ASTER Remote Sensing Imagery

Mastoureh Yousefi <sup>1,\*</sup>, Seyed Hassan Tabatabaei <sup>1,\*</sup> , Reyhaneh Rikhtehgaran <sup>2</sup>, Amin Beiranvand Pour <sup>3,\*</sup>  and Biswajeet Pradhan <sup>4,5,6</sup> 

<sup>1</sup> Department of Mining Engineering, Isfahan University of Technology, Isfahan 84156-83111, Iran; m.usefi@mi.iut.ac.ir

<sup>2</sup> Department of Mathematical Sciences, Isfahan University of Technology, Isfahan 84156-83111, Iran; r\_rikhtehgaran@cc.iut.ac.ir

<sup>3</sup> Institute of Oceanography and Environment (INOS), University Malaysia Terengganu (UMT), Kuala Nerus 21030, Terengganu, Malaysia

<sup>4</sup> Centre for Advanced Modelling and Geospatial Information Systems (CAMGIS), Faculty of Engineering & IT, University of Technology Sydney, Sydney 2007, Australia; Biswajeet.pradhan@uts.edu.au

<sup>5</sup> Center of Excellence for Climate Change Research, King Abdulaziz University, P.O. Box 80234, Jeddah 21589, Saudi Arabia

<sup>6</sup> Earth Observation Centre, Institute of Climate Change, University Kebangsaan Malaysia, Bangi 43600, Selangor, Malaysia

\* Correspondence: tabatabaei@cc.iut.ac.ir (S.H.T.); beiranvand.pour@umt.edu.my (A.B.P.); Tel.: +98-3133915104 (S.H.T.); +60-9-6683824 (A.B.P.); Fax: +60-9-6692166 (A.B.P.)



**Citation:** Yousefi, M.; Tabatabaei, S.H.; Rikhtehgaran, R.; Pour, A.B.; Pradhan, B. Application of Dirichlet Process and Support Vector Machine Techniques for Mapping Alteration Zones Associated with Porphyry Copper Deposit Using ASTER Remote Sensing Imagery. *Minerals* **2021**, *11*, 1235. <https://doi.org/10.3390/min1111235>

Academic Editor: Paul Alexandre

Received: 2 September 2021

Accepted: 4 November 2021

Published: 6 November 2021

**Publisher's Note:** MDPI stays neutral with regard to jurisdictional claims in published maps and institutional affiliations.



**Copyright:** © 2021 by the authors. Licensee MDPI, Basel, Switzerland. This article is an open access article distributed under the terms and conditions of the Creative Commons Attribution (CC BY) license (<https://creativecommons.org/licenses/by/4.0/>).

**Abstract:** The application of machine learning (ML) algorithms for processing remote sensing data is momentous, particularly for mapping hydrothermal alteration zones associated with porphyry copper deposits. The unsupervised Dirichlet Process (DP) and the supervised Support Vector Machine (SVM) techniques can be executed for mapping hydrothermal alteration zones associated with porphyry copper deposits. The main objective of this investigation is to practice an algorithm that can accurately model the best training data as input for supervised methods such as SVM. For this purpose, the Zefreh porphyry copper deposit located in the Urumieh-Dokhtar Magmatic Arc (UDMA) of central Iran was selected and used as training data. Initially, using ASTER data, different alteration zones of the Zefreh porphyry copper deposit were detected by Band Ratio, Relative Band Depth (RBD), Linear Spectral Unmixing (LSU), Spectral Feature Fitting (SFF), and Orthogonal Subspace Projection (OSP) techniques. Then, using the DP method, the exact extent of each alteration was determined. Finally, the detected alterations were used as training data to identify similar alteration zones in full scene of ASTER using SVM and Spectral Angle Mapper (SAM) methods. Several high potential zones were identified in the study area. Field surveys and laboratory analysis were used to validate the image processing results. This investigation demonstrates that the application of the SVM algorithm for mapping hydrothermal alteration zones associated with porphyry copper deposits is broadly applicable to ASTER data and can be used for prospectivity mapping in many metallogenic provinces around the world.

**Keywords:** porphyry copper deposits; ASTER; machine learning; DP; SVM; SAM

## 1. Introduction

Because of the importance of minerals in industry and other aspects of human life, appropriate methods to explore minerals are essential. The use of remote sensing data to obtain information from far objects is one of the most significant technologies in this century. Remote sensing satellite imagery is extensively used in different sectors of Earth

science such as mineral mapping [1–4]. The results of remote sensing studies, by means of saving time and cost in identifying alteration zones, have greatly contributed to the exploration of minerals, especially in the reconnaissance stages [5–8].

In recent decades, remote sensing has been used successfully in the identification of lithological units, structure features, and alterations zones with the development of new algorithms and ML techniques [9–11]. Owing to the high volume of remote sensing satellite data, data mining methods to extract the desired information are necessary [12,13]. Classification algorithms undoubtedly play an essential role in analyzing multidimensional data such as multispectral and hyperspectral images. Depending on need, different classification methods have been used for mineral mapping. These methods are generally divided into three categories: supervised, unsupervised, and semi-supervised. Supervised methods such as spectral angle mapping (SAM), support vector machines (SVM), and maximum likelihood (ML) have been widely used for remote sensing data processing with the aim of geological mapping [14,15]. The SVM method in the field of mineral mapping has been considered over the past two decades [16,17]. Clustering or unsupervised methods divide the data into groups to have the most similarity in each group and the least similarity between the groups [18]. Unlike supervised methods, these methods are less commonly used for remote sensing data processing in mineral exploration. For mineral exploration, clustering methods are usually used in conjunction with supervised methods to obtain better results. Semi-supervised methods aim to improve the results by combining these two methods [19]. Different clustering methods are used in various sciences, such as data mining, pattern recognition, image clustering, etc. [20]. These methods do not require training data. These methods are divided into two main categories: model-based and non-model-based. In non-model-based methods, the only parameter that needs to be known initially is the number of clusters [21]. Determining the number of clusters is a significant challenge that can be problematic in clustering big data [22]. Model-based methods do not even need to determine the number of clusters and can cluster the data without any information.

Despite proper performance in identifying minerals and alterations using supervised methods, preparing and selecting appropriate training data from them is costly and time-consuming. In this research, an attempt has been made to determine appropriate training data based on the nature of the data, using an approach consisting of clustering and classification methods. Then, using this training data for the supervised methods, identical areas in terms of alteration were identified. In this study, the basic model of the DP method was used to cluster the alteration zones of the Zefreh porphyry copper deposit, the UDMA, central Iran, using ASTER data. Then the results of this clustering were used as training data to identify corresponding alteration zones using the SVM method. The specific objectives of this research are: (i) to detect alteration zones in the Zefreh porphyry copper deposit using RBD, LSU, OSP, SFF algorithms; (ii) to determine the exact expansion of alteration zones in the Zefreh porphyry copper deposit using the DP method and use its results as training data for supervised methods; (iii) to perform SVM and SAM methods using training data obtained from the DP method and specify analogous alteration areas in the ASTER scene; and (iv) to verify the classification results using field checking of alteration zones.

## 2. Geology of the Study Area

The Zefreh porphyry copper deposit is located in the UDMA belt of central Iran, northeast (65 km) of Isfahan province. The location is bounded by latitudes  $33^{\circ}03'9.35''$  N and  $33^{\circ}03'54.5''$  N and longitudes  $52^{\circ}13'38.48''$  and  $52^{\circ}14'25.88''$  E (Figure 1a,b). The copper deposit is related to the Qom-Zefreh fault and its placement in the UDMA belt. Mechanism of movement of Qom-Zefreh and Naein-Baft and tensile performance between these two tectonic lineaments has led to the creation of longitudinal sliding tensile basins in the Zefreh region [23]. Crustal stretching along these strike-slip faults has facilitated the ascent and replacement of intrusive masses and the formation of dikes and the concentration of

several mineralogical hydrothermal systems such as the Zefreh porphyry copper deposits, Kahang, Zafarqand, and the Kalchoye epithermal deposits, which are related to these two tectonic lineaments [23]. Volcanic activity in the Zefreh region occurred from the Eocene to the Miocene. Pyroclastic and andesitic lavas in the eastern, southeastern, and southwestern parts of the area are the oldest rock units in the region. These units have been altered to propylitic as a result of magmatic activity. In the central part, in the Late Eocene dacites, phyllic and argillic alterations zones are observed. Granodiorite subvolcanics are presented in the northeastern, penetrating dacite, pyroclastic, and andesitic lavas. In these stocks, weak potassium alteration and abundant quartz-magnetite veins are observed [24,25].

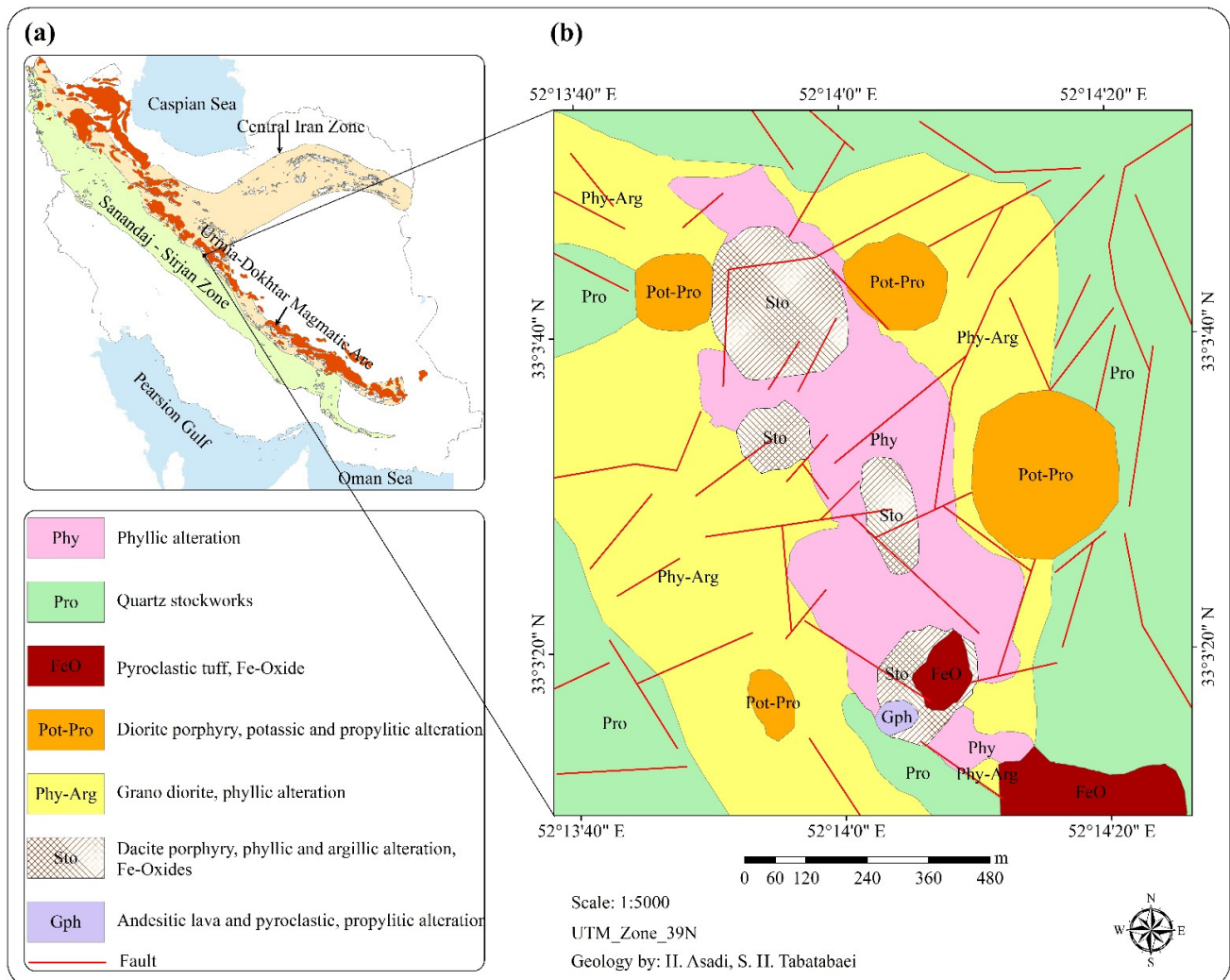


**Figure 1.** (a) The geographical location of the Zefreh area in the UDMA belt of central Iran; (b) geological map of the Zefreh area (scale 1:5000).

### 3. Materials and Methods

#### 3.1. Data Characteristics

In this study, ASTER Level 1 T (Precision Terrain Corrected Registered At-Sensor Radiance) data were used. The ASTER sensor is a multispectral imager on NASA's Terra platform. ASTER has 14 bands in three subsystems, the visible and near infrared (VNIR) (3 bands), the shortwave infrared (SWIR) (6 bands), and the thermal infrared (TIR) (5 bands), in the range of 0.52–11.65  $\mu\text{m}$ . The ASTER image has a spatial resolution of 15 m in the VNIR bands, 30 m in the SWIR bands, and 90 m in the TIR bands [26]. ASTER satellite imagery was designed based on geological needs, and it has been very efficient in this

field over the last two decades [27]. ASTER data have an appropriate spectral and spatial resolution in the SWIR range, where many alteration minerals can be distinguished [8,9]. ASTER SWIR detectors are no longer functioning due to anomalously high SWIR detector temperatures. ASTER SWIR data acquired since April 2008 are not usable and show saturation of values and severe striping. However, VNIR and TIR data continue to show excellent quality, meeting all mission requirements and specifications. ASTER images can be downloaded from the "<https://search.earthdata.nasa.gov/>" site. To download the ASTER data, the ASTER granule ID can be found in the "<https://earthexplorer.usgs.gov/>" site.

The ASTER image used in this study was acquired on 11 March 2008. This ASTER scene covers the Zefreh porphyry copper deposit in the UDMA of central Iran. The image has 1% cloud coverage and is suitable for a remote sensing study. In this study, the nine bands of the VNIR and SWIR subsystems were stacked and used. The 30 m resolution SWIR of the ASTER data was re-sampled to correspond to the VNIR 15-m spatial dimensions. Nearest neighbor re-sampling method was applied to preserve the original pixel values in the re-sampled image. Radiometric and geometric corrections had been already applied on the ASTER L1T level data used in this study. ASTER data were also georeferenced and orthorectified [28]. The necessary preprocessing of this data included atmospheric correction and vegetation removal, which were subsequently done. Internal Average Relative Reflectance (IARR) correction was used to eliminate atmospheric effects. The IARR technique is recommended for mineralogical mapping as a preferred calibration technique in arid and semi-arid regions, because it does not require the prior knowledge of samples collected from the field [29]. Parts of the image that contained vegetation were identified with the NDVI index [30], and values greater than 0.3 were masked so that the results were not affected by vegetation reflectance. Figure 2 show the flowchart of the methodology used in this study.

### 3.2. Methods

#### 3.2.1. Dirichlet Process (DP)

Owing to the nature of alterations, which are composed of different minerals with different values, their values can be modeled as distributions and can be separated from each other through the distribution of their compounds. In other words, different alterations can be separated into separate clusters. In this research, the DP method, which is based on the distribution over the dispersal of parameters, was used to model different alterations. In addition to the expected results, the advantage of using this method is that there was no need to determine the number of clusters.

In this study, considering that the DP clustering algorithm was implemented on the image in the Zefreh area with different lithologies, we assumed that each type of lithology was a multivariate normal distribution. Because each lithology was composed of a number of minerals with different compositions that have different spectral characteristics, we also considered their distribution to be normal. Because of the complexity of the composition of lithologies and their constituent minerals, we considered a hierarchical structure for the model parameters to fit well with the data structure.

The DP method is a non-parametric Bayesian method. DP was first introduced in 1973 by Ferguson [31]. This method was then developed and used in various sciences [32–34]. Mixed model DP uses a database distribution to model data that are mixed from several clusters. DP is generally formulated using Equation (1), but the number of model parameters is not fixed and can be changed as needed.

$$\begin{aligned}
 G &\sim \text{DP}(\alpha, G_0) \\
 \theta_{z_i} &\sim G \\
 P(z_i = k) &= \pi_k \\
 z_i &\sim \text{cat}(\pi_k) \\
 x_i | z_i, \theta_{z_i} &\sim F(\theta_{z_i}) \quad i = 1 : n
 \end{aligned} \tag{1}$$

where,  $G$  and  $G_0$  are the distributions on the  $\theta$  parameter.  $G_0$  is the base distribution, and  $\alpha$  is the concentration parameter of the Dirichlet distribution (Equation (1)). This parameter controls the degree of similarity of the  $G$  distribution to the base distribution. It is also effective in assigning a new sample to the previous cluster or being in a new cluster [35,36]. Equation (1) has a hierarchical structure so that each parameter is obtained from the posterior distribution of another parameter.  $\theta$  is the parameter of data distribution. This study assumed that the values of each pixel  $x_i$  are a mixture of several clusters, and  $\pi_k$  is the mixing proportion of each cluster ( $k$ ). The value of  $z_i$  was obtained from the categorical distribution on  $\pi_k$ .

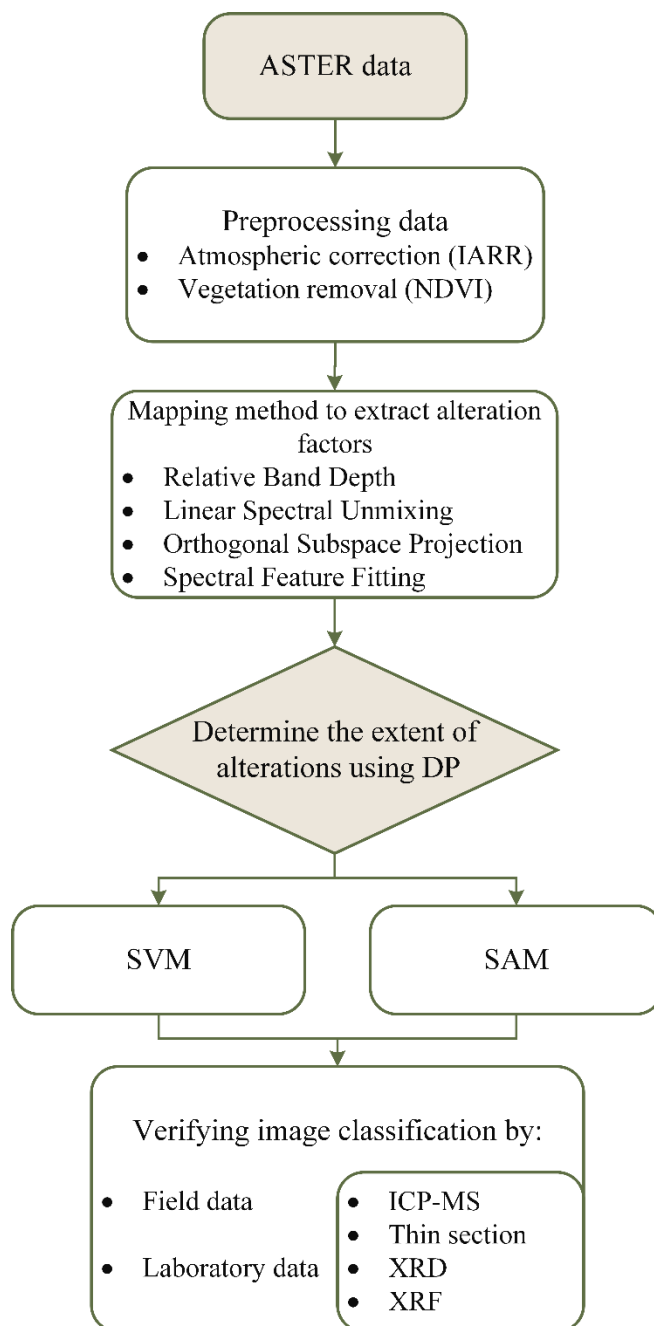


Figure 2. An overview of methodological flowchart used in this study.

Then Equation (2) was used to classify each data point (in this study, each pixel) in an existing cluster or a new cluster.

$$P(z_i = z | z_{-i}, x_{-i}, \theta) \propto \begin{cases} \frac{N_{-i,z}}{N-1+\alpha} F(x_i, \theta_c) & \text{if } c \text{ exist} \\ \frac{\alpha}{N-1+\alpha} \int F(x_i, \theta) dG_0(\theta) & \text{new } c \end{cases} \quad (2)$$

Several methods have been proposed in the literature to represent DP, including the Stick-Breaking (SB), Chinese restaurant, and, the Polya urn [35,37]. Here, the SB process was used for the probability of each cluster (Equation (3)). Each part of the SB models the probability of mixing proportions. In Equation (3),  $\beta$  is the beta distribution.

$$\begin{aligned} \pi_1 &= \beta_1 \\ \pi_k &\sim \beta_k \prod_{j=1}^{k-1} (1 - \beta_j) \sum_{j=1}^k \pi_j = 1 \\ \beta_k &\sim \text{Beta}(1, \alpha) \quad k = 2, 3, \dots \end{aligned} \quad (3)$$

As mentioned before, this method is non-parametric, and after constructing the model that fit the data, we were faced with several unknown parameters where the Markov chain Monte Carlo (MCMC) simulation was used to find their values. Using MCMC methods, the number of unknown quantities based on posterior probability is simulated in an acceptable way [38] (Equation (4)).

$$p(\theta, \pi | x_1, \dots, x_n) \propto \prod_{i=1}^n \left\{ \sum_{j=1}^k \pi_j f(x_i | \theta_j) \right\} p(\theta) p(\pi) \quad (4)$$

### 3.2.2. Support Vector Machine (SVM)

Geo-computational methods for mapping minerals in satellite images, analysis of geochemical, geophysical data, etc., are kinds of classification because each method aims to find a prospect or non-prospect area [39]. SVM is one of the classification methods used to classify high-dimensional data and is suitable for cases where a limited number of training data are available [40].

The SVM algorithm was first used by [41] as a supervised method. Other studies have used this method as an unsupervised method [42], and a semi-supervised method [43] for clustering and classification. This method uses a hyperplane to separate the data (background value from an anomaly or desired from undesirable), which maximizes the margin between classes. SVM uses the pairwise classification strategy for multiclass classification. Suppose we have  $x_i \in R^n \quad i = 1, \dots, n$  educational data vectors (in this study, we had  $n$  as the number of pixels with dimension  $P$ ) so that each pixel belongs to the class  $y_i \in \{-1, 1\}$ . Multiple hyperplanes can be used to separate data; a hyperplane with the maximal margin from the most external data of each class (Support vectors) is desirable.

This hyperplane can be formulated as follows [39]:

$$f(X) = \text{sgn}(W^T X + b), \quad (5)$$

$$\text{sgn}(X) = \begin{cases} 1 & \text{if } x > 0 \\ 0 & \text{if } x = 0 \\ -1 & \text{if } x < 0 \end{cases} \quad (6)$$

The soft margin is used to obtain the parameters  $w$  and  $b$  by considering the variable  $\xi_i$  and the penalty function  $C$  (Equations (7) and (8)). This hyperplane permits the misclassification of some data in a controlled condition [44]:

$$\begin{aligned} & \text{Minimize} \quad \frac{1}{2} \|w\|^2 + C \sum_{i=1}^n \xi_i \\ \text{Subject to} \quad & \begin{cases} y_i (W^T X_i + b) \geq 1 - \xi_i & i = 1, \dots, n \\ \xi_i \geq 0 & i = 1, \dots, n \end{cases} \end{aligned} \tag{7}$$

$$\text{Minimize} \quad L(W, b, \alpha) = \frac{1}{2} \|W\|^2 - \sum_{i=1}^n \alpha_i y_i (W \cdot X_i + b) + \sum_{i=1}^n \alpha_i \tag{8}$$

To minimize Equation (8) concerning  $W$  and  $b$ , we obtained the derivative of the above equation with respect to these variables (Equation (9)). Finally, we arrived at the following equations by placing the results (Equation (10)). By converting the problem to a quadratic programming problem and calculating the Lagrangian multipliers (Equation (11)), the problem is solved by finding the saddle point [39,44]:

$$\frac{\partial L}{\partial W} = 0, \quad \frac{\partial L}{\partial b} = 0 \tag{9}$$

$$W = \sum_{i=1}^n \alpha_i y_i X_i \quad \sum_{i=1}^n \alpha_i y_i = 0 \tag{10}$$

$$\text{Maximize} \quad L(\alpha) = \sum_{i=1}^n \alpha_i - \frac{1}{2} \sum_{i,j=0}^n \alpha_i \alpha_j y_i y_j X_i \cdot X_j = 0 \tag{11}$$

$$\text{Subject to} \quad \alpha_i \geq 0, \quad i = 1, \dots, n, \quad \sum_{i=1}^n \alpha_i y_i = 0 \tag{12}$$

$$f(x) = \text{sgn} \left( \sum_{i,j=1}^n \alpha_i y_i (X_i X_j) + b \right) \tag{13}$$

In high-dimensional data, classification will be difficult. One way to overcome this problem is to use a kernel to transfer data to another feature space to make class separations easier and better. In this study, the Radial Basis Function (RBF) kernel was used (Equation (14)), which studies show has a better performance in this field. This kernel is like the K-nearest neighbor. It has all the advantages of a K-nearest neighbor. In addition, because it only needs to save support vectors instead of entire data it reduces space and complexity [45,46]. Finally, the decision function is changed as follows [44,47] (Equation (15)).

$$K(X_i, X_j) = e^{-\gamma(X_i - X_j)^2} \tag{14}$$

$$f(x) = \text{sgn} \left( \sum_{i,j=1}^n \alpha_i y_i K(X_i, X_j) + b \right) \tag{15}$$

### 3.2.3. Spectral Angle Mapper (SAM)

The SAM classification method is one of the most widely used methods in mineral mapping. The library spectrum, field spectrum, and image spectrum can be used for training or reference data in this method. Each pixel is considered a multidimensional vector with dimensions equal to the number of bands [48]. In the SAM method, the similarities between training or known data and test data in  $n$ -dimensional space are calculated with the angle between their spectra [48,49]. In this method, the direction of

the spectra vectors is substantial, not their length, so the difference of light intensity in different parts of the image does not affect processing.

$$\text{SAM} = \arccos \left( \frac{\langle \mathbf{I}_{\{k\}} \cdot \mathbf{J}_{\{k\}} \rangle}{\|\mathbf{I}_{\{k\}}\| \|\mathbf{J}_{\{k\}}\|} \right). \quad (16)$$

In Equation (16),  $\mathbf{I}_{\{k\}}$  is the spectrum vector of the known data (in this study, Zefreh training data), and  $\mathbf{J}_{\{k\}}$  is the spectrum vector of the ASTER scene case study.  $\langle \cdot \cdot \rangle$  indicates the scalar multiplication.  $\|\cdot\|$  is the vector's norm [50,51].

### 3.2.4. Laboratory Analysis

Inductively coupled plasma–mass spectrometry (ICP-MS) analysis is one of the most accurate methods for measuring the value of elements in the selected samples. This analysis can detect and measure values less than one per billion (ppb). The input of the ICP-MS device must be a solution without suspended particles. The sample solution is sprayed into a plasma torch. The argon gas plasma ionizes the solution's molecules in the ICP. An electric field then accelerates these ions. Accelerated ions enter a magnetic field in the ICP device. The ions in the magnetic field are separated based on the charge-to-mass ratio, and the device can measure the value of each ion [52]. In this study, the collected rock samples were analyzed using a Perkin Elmer Sciex ELAN 9000 ICP-MS for some trace elements. The X-ray fluorescence (XRF) measured the value of sample compounds by bombarding the sample with X-rays or gamma rays and measuring the emission characteristic [53]. A Philips PW1480 XRF spectrometer was used in this study for measuring the percentage of major oxides in the selected rock samples. The samples were analyzed in the Zarazma Laboratory, Tehran, Iran. The results of these analysis are presented in Appendix A, Tables A1 and A2.

The thin section was a microscopic cut of rock, thickness between 25–30  $\mu\text{m}$ , both sides were covered with glass slides. Thin sections were used for petrographic studies by optical microscopy. Quartz and feldspars should be gray to white in cross-polarized light in standard thin sections [54,55]. In this study, thin sections of alteration zones and lithological units were prepared. Thin sections were studied using the Kyowa ME-POL2 microscope (made in Japan) at magnification 20 in the Isfahan University of Technology, Iran. X-ray diffraction (XRD) was used to identify the crystal structure and major and minor minerals in a sample. In this method, the X-ray beam was irradiated to the sample, and the output diffraction pattern determined the type of mineral [56]. An ASENWARE/AW-XDM300 XRD diffractometer was used for measuring the important minerals in the sample collected in this study (Appendix A, Table A3). The XRD analysis was also performed in the Zarazma Laboratory, Tehran, Iran.

## 4. Results and Analysis

### 4.1. Determining the Training Data

In order to accurately determine the training data to use in the SVM and SAM algorithms, firstly, the alteration zones were identified by several mapping methods such as RBD, LSU, OSP, and SFF [57–60]. Then the exact extent of each alteration zone in the Zefreh porphyry copper deposit was determined using the DP algorithm.

### 4.2. Detection of the Alteration Zones

In each alteration, several indicator minerals had a specific spectral signature that made it possible to identify them in remote sensing images and determine the type of alteration. According to the kind of alteration, the location of enrichment elements and mineralization was identified. In this study, we used RBD, LSU, OSP, and SFF mapping methods to reveal phyllic, argillic, and propylitic alterations in the Zefreh porphyry copper deposit. Figure 3a shows an RGB color composite (R:3, G:2, B:1) of the ASTER full scene covering the study area.

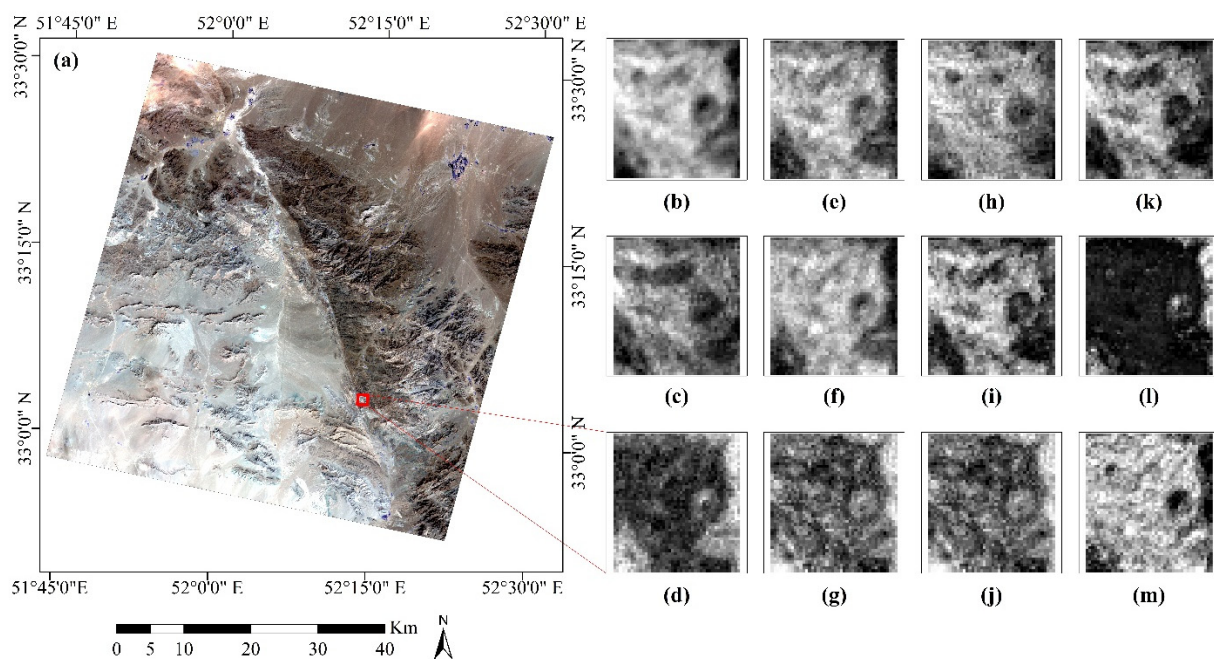


**Figure 3.** (a) Color composite of ASTER (R:3, G:2, B:1); (b–d) Phyllic, argillic and propylitic alteration results of the RBD method; (e–g) alteration results of the LSU method; (h–j) show mapping of phyllic, argillic and propylitic alterations using the OSP; (k,l) are the results of the SFF method; (m) shows the Fe-oxide alteration.

In the RBD method, considering the points of absorption and reflectance of mineral spectra, to determine the alterations, the band ratios  $(B7 + B5)/B6$  for phyllic, the ratio  $(B7 + B4) / B5$  for the argillic, and the ratio  $(B7 + B9)/B8$  for propylitic alterations were used [61,62] (Figure 3b–d). To identify the alterations using LSU or SFF methods, the reference spectra related to the indicator minerals of each alteration zones were extracted from the USGS spectral library [63]. Figure 4 shows the USGS spectral of the indicator minerals after re-sampling to the ASTER band-passes. The phyllic alteration zone included sericite, illite, pyrite, and quartz [64]. The sericite mineral spectral signature was considered for mapping the phyllic zone. The argillic zone accumulated clay minerals, including illite, kaolinite, montmorillonite, alunite, halloysite, and quartz [64]. Argillic was identified by representative spectra of kaolinite and montmorillonite. The propylitic alteration zone consisted of epidote, calcite, and chlorite minerals, and was characterized mainly by the spectral signature of chlorite and epidote minerals [65]. Implementing the LSU method on the ASTER subset of the Zefreh porphyry copper deposit, the regions containing the indicator minerals manifested as bright pixels (Figure 3e–g). These images showed the mapping of phyllic, argillic, and propylitic alteration zones, respectively. LSU assumed that the value of each pixel was a linear combination of its endmembers in the fraction of endmembers with noise [57]. By projecting the pixel vector of the image in the subspaces, the OSP method eliminated the undesirable effects by increasing the signal-to-noise ratio, determining the spectral signature of the desired indicator mineral [66]. The results of the OSP method are shown in Figure 3h–j. The SFF method identified the desired areas by comparing the image spectrum with the spectral library spectrum, performing the least squares fitting, and selecting the best fit [48]. The SFF method showed acceptable results only for the phyllic and propylitic alteration (Figure 3k,l). The  $B2/B1$  band ratio was used for mapping iron oxides (Figure 3m).

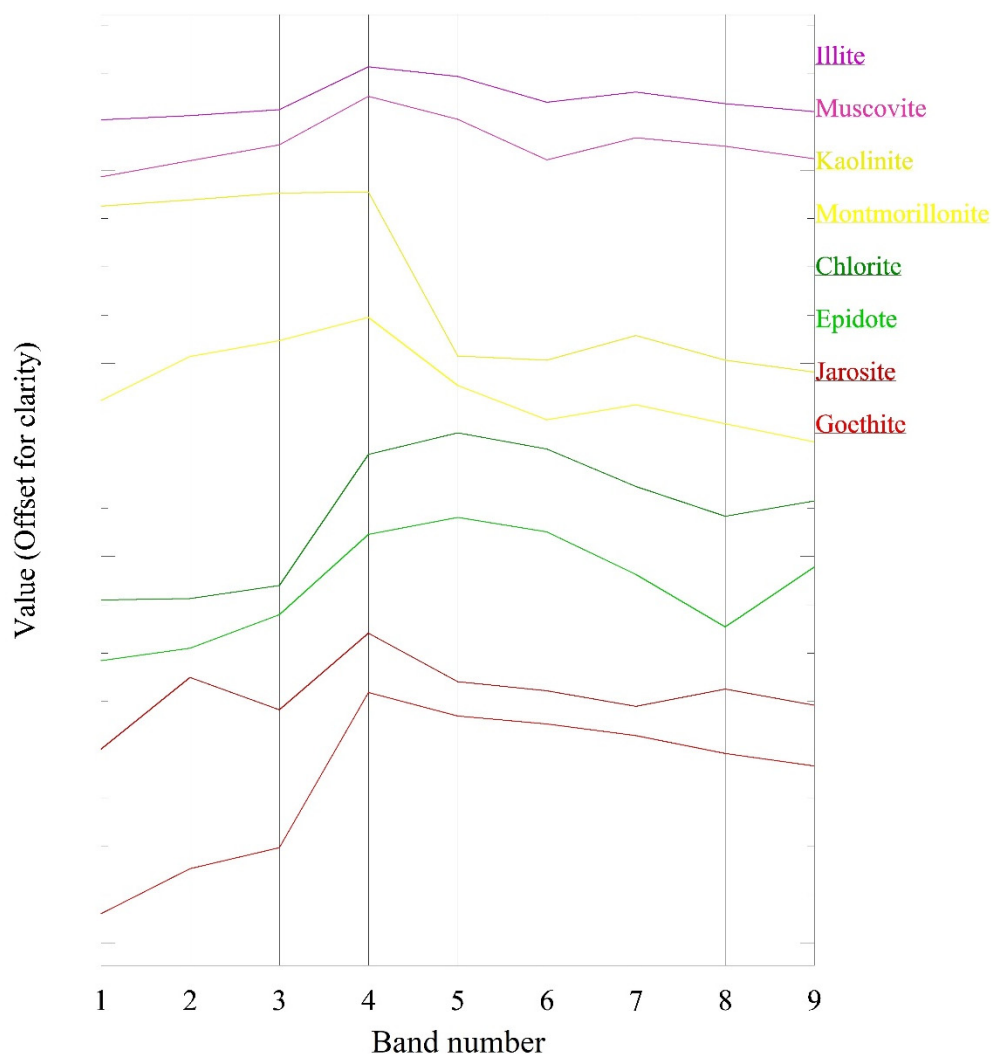


**Figure 4.** The spectral signatures (reflectance spectra) of indicator alteration minerals selected from the USGS spectral library that was re-sampled to the ASTER band-passes.

#### 4.3. Implementation of the DP Method on the Zeftreh Area

The results obtained from different alteration mapping methods (Figure 3) were used as input to the implementation of the DB method. Using the DP method, the digital number (DN) value of the distribution of the pixels was assumed to be Gaussian. Considering the fact that rocks are composed of minerals and minerals are composed of elements, the DN values of each pixel were modeled as distributions over dispersals. This means that the value of each pixel ( $X_i$ ) was considered a normal distribution with a distinct mean and variance. The number of different distributions was equal to the number of clusters. It was assumed that the mean value of these distributions had a normal distribution (base distribution) (Equations (17) and (18)). Gaussianness of data distribution is not required, and if the data distribution is not normal, the results will not be much different. As mentioned in Section 3.2.1, this method is a non-parametric method where, after defining the model and implementing it in the Bayesian inference Using Gibbs Sampling (BUGS) software, unknown parameters including the mean and variance of data distribution, probability of each cluster, and the number of clusters were identified by the MCMC simulation method. The BUGS was first released by Smith and Gelfand [67].

The parameter values were obtained after 3000 times MCMC simulation and removing the first 1000 unstable values (Figure 5a,b). The number of simulations varies and should continue until the value of the parameters converges.

$$X_i \sim \text{Normal}(\mu_1(C_i), \sigma_1(C_i)), \quad (17)$$

$$\mu_1(C_i) \sim \text{Normal}(\mu_2, \sigma_2), \quad (18)$$

$$C_i \sim \text{Categorical}(P(1 : C)), \quad (19)$$

$$\sigma_1(C_i) \sim \text{Wishart}(R). \quad (20)$$

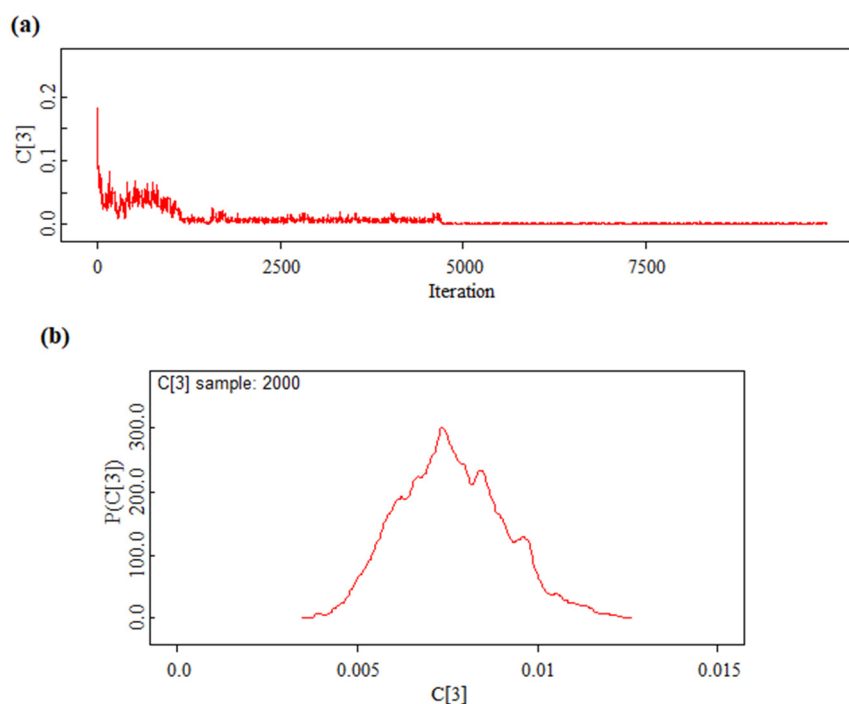


**Figure 5.** (a) MCMC simulation history of the C parameter to achieve convergence. (b) The posterior distribution of the parameter.

In the above equations,  $X_i$  specifies the DN value of each pixel,  $C_i$  is the categorical distribution of the probability occurrence of each cluster.  $\mu$  and  $\sigma$  show the mean and variance of the normal distribution, respectively (in BUGS software, precision is used instead of variance). The precision value is calculated from the Wishart distribution [68,69].

The result of the implementation of the DP algorithm was the clustering of the ASTER image in Figure 6. The alteration zones in this image were more accurate than the geological map because the alteration zones were detected by the approach applied in this analysis. Therefore, the results of this clustering as training data provided more significant results compared to the existing geological map (Figure 1). Hence, the result of DP was used as the training data in the SVM and SAM supervised methods. The result of this clustering was five distinct clusters, and by adapting them to the geological map, we determined which kind of alterations defined each cluster. Figure 6 indicates that the areas showing the potassic zone were also mapped. This zone was not used as training data because the potassic spectra were not easily detectable in the SWIR and VNIR bands of ASTER. Mapping the potassic zone can be performed using the TIR bands, which was not considered in this analysis.

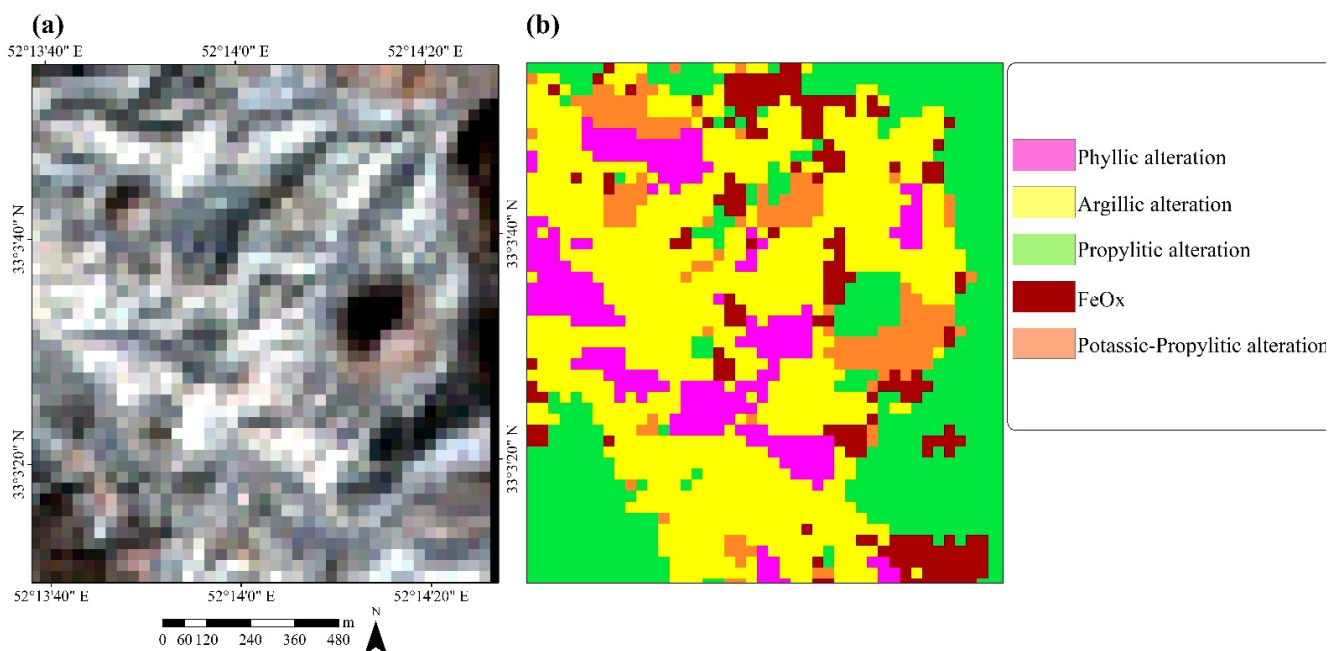


**Figure 6.** (a) The Zefreh ASTER image, (b) the DP clustering method results showing the spatial distribution of alteration zones in the study area.

#### 4.4. Implementation of the SVM on ASTER Data

The alteration zones derived from the DP were used as training data to find similar alteration zones in the ASTER scene. We used the RBF kernel to transfer data to other spaces and classify the data. In the SVM method, the  $\gamma$  parameter and the penalty parameter must be defined. These parameters were optimized on the training data using the genetic algorithm in MATLAB software. The optimal values of the penalty and  $\gamma$ , 0.211 and 2, respectively, were obtained. Finally, the SVM algorithm was implemented on the ASTER image using the specified parameters and the training data using ENVI (Environment for Visualizing Images, <http://www.exelisvis.com>) version 5.3 software package (L3Harris Technologies, Melbourne, FL, USA). The results of this classification for phyllic, argillic and propylitic alterations are shown in Figure 7a–d.

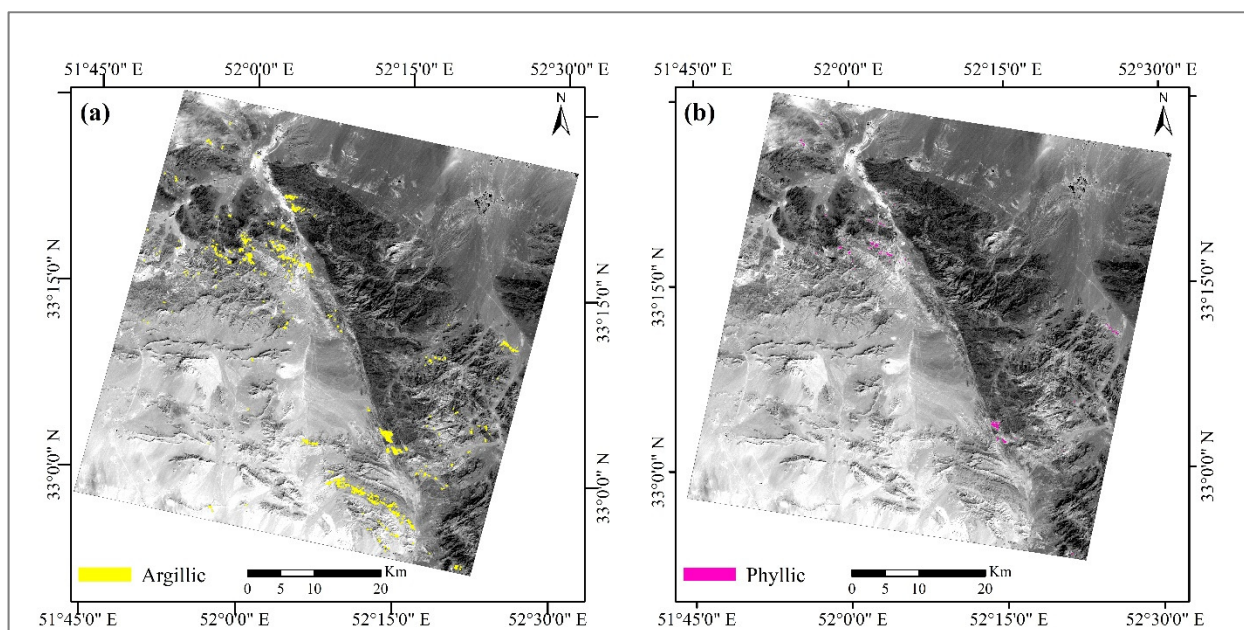


**Figure 7.** Cont.

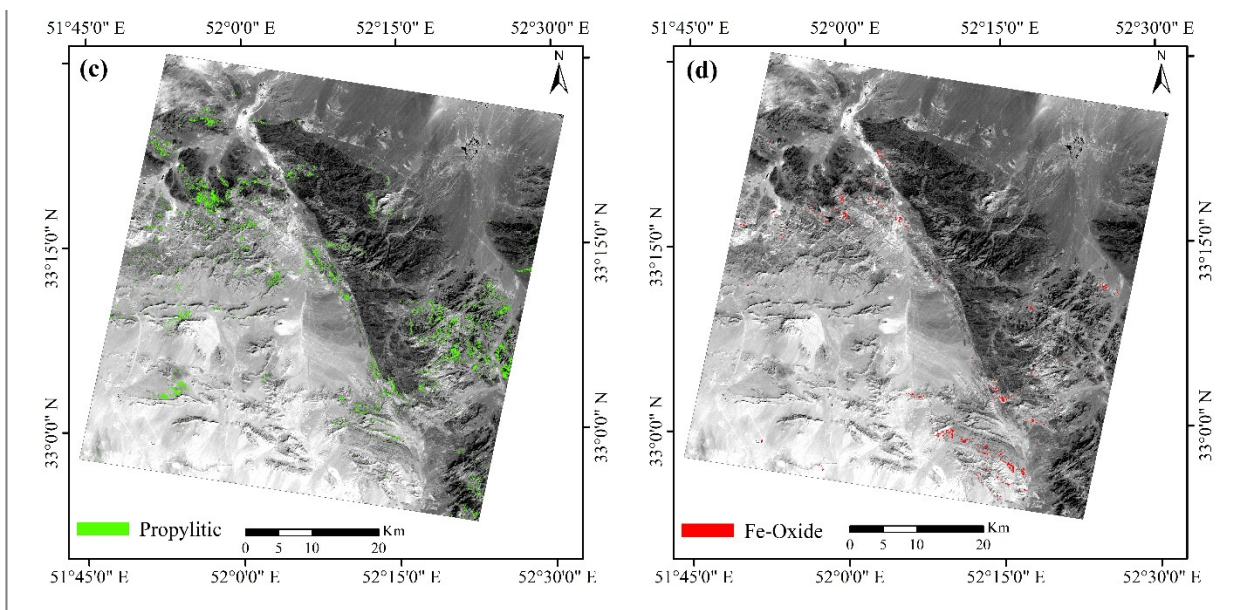


**Figure 7.** The results of SVM on the ASTER data. (a) Argillic alteration, (b) phyllic alteration, (c) propylitic alteration, and (d) Fe-oxide alteration.

#### 4.5. Implementation of the SAM on ASTER Data

The SAM classification was used to compare the efficiency of the SVM results. DP clustering data was used as the training data for this algorithm. Phyllic, argillic, and propylitic alteration zones were mapped using the SAM algorithm on the ASTER image. The selected SAM spectral angles (in radians) used in this study were:  $\alpha = 0.4$  for phyllic alteration,  $\alpha = 0.25$  for argillic, and  $\alpha = 0.3$  for propylitic. The results of the SAM classification are shown in Figure 8a–d.

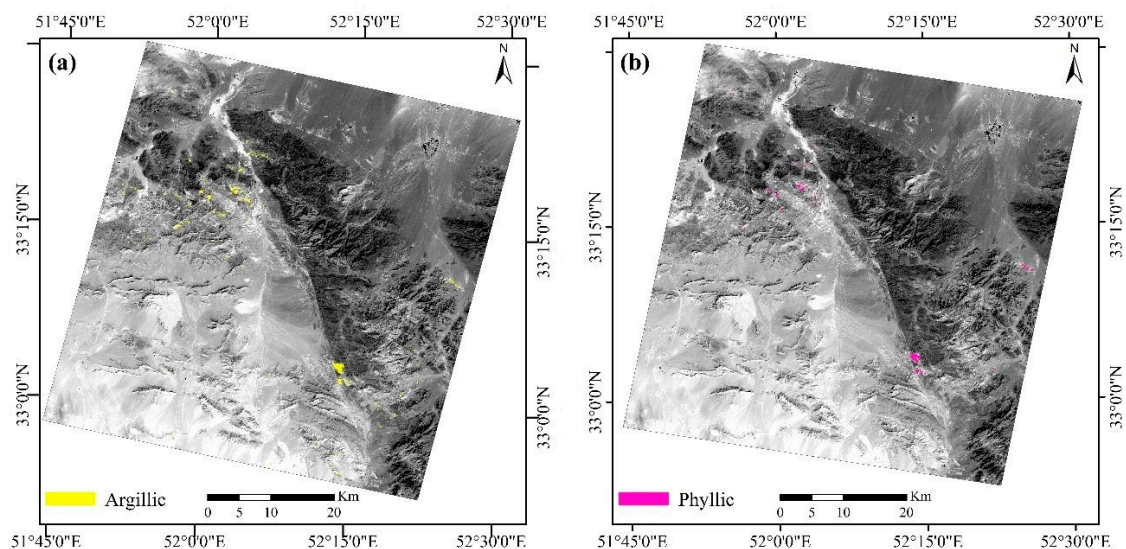


**Figure 8.** Cont.

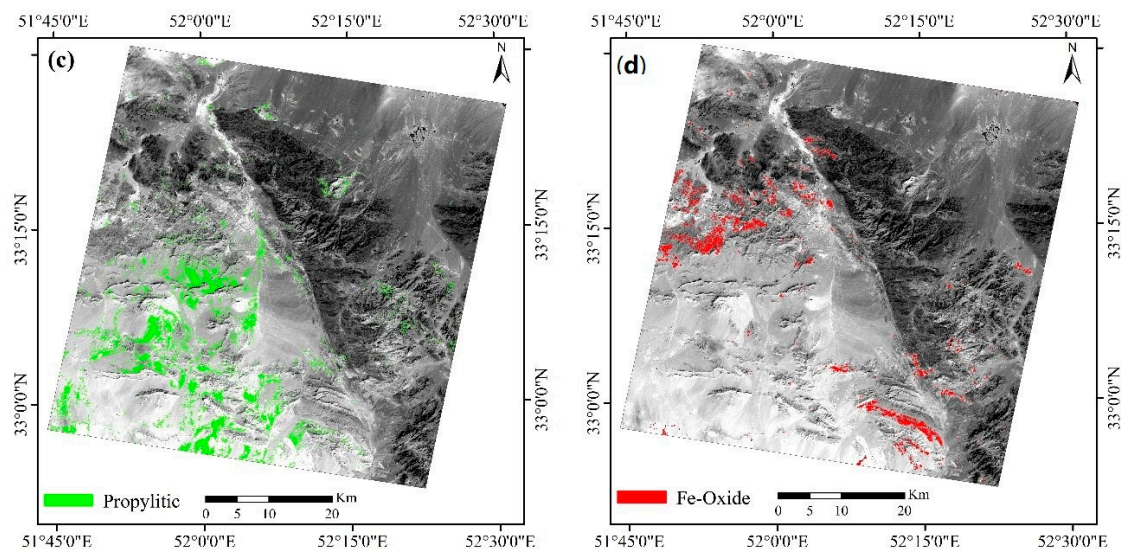


**Figure 8.** The results of SAM spectral mapping on the ASTER data. (a) Argillic alteration, (b) phyllic alteration, (c) propylitic alteration, and (d) Fe-oxide alteration.

### 5. Fieldworks

To validate the classification results, the field survey was performed by considering the following records: (i) the areas where the results of SVM showed the distribution of several alteration zones, especially phyllic and argillic; (ii) rock units of the mineralization zone; and (iii) areas where faults and ring structures were identified. In the field survey, 21 rock samples were collected by bulk sampling method for ICP-MS analysis, thin section, XRD and XRF. The location of sampling points was recorded with a handheld GPS (Garmin eTrex 30x; average accuracy of 3 m; made in Taiwan). The results of ICP-MS, XRF, and XRD are presented in Appendix A, Tables A1–A3. Figures 9 and 10 show the location of the sampling points on the SVM and SAM alteration maps, respectively.

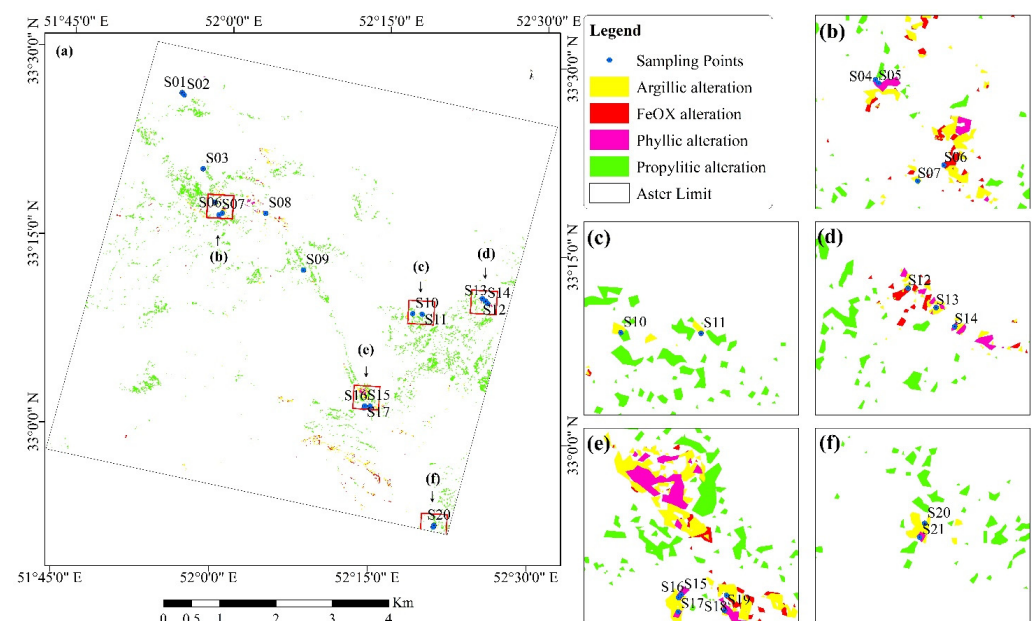


**Figure 9.** The results of SVM spectral mapping on the ASTER data. (a) ASTER full scene of the study area. (b–f) Selected subsets for sampling and field survey.

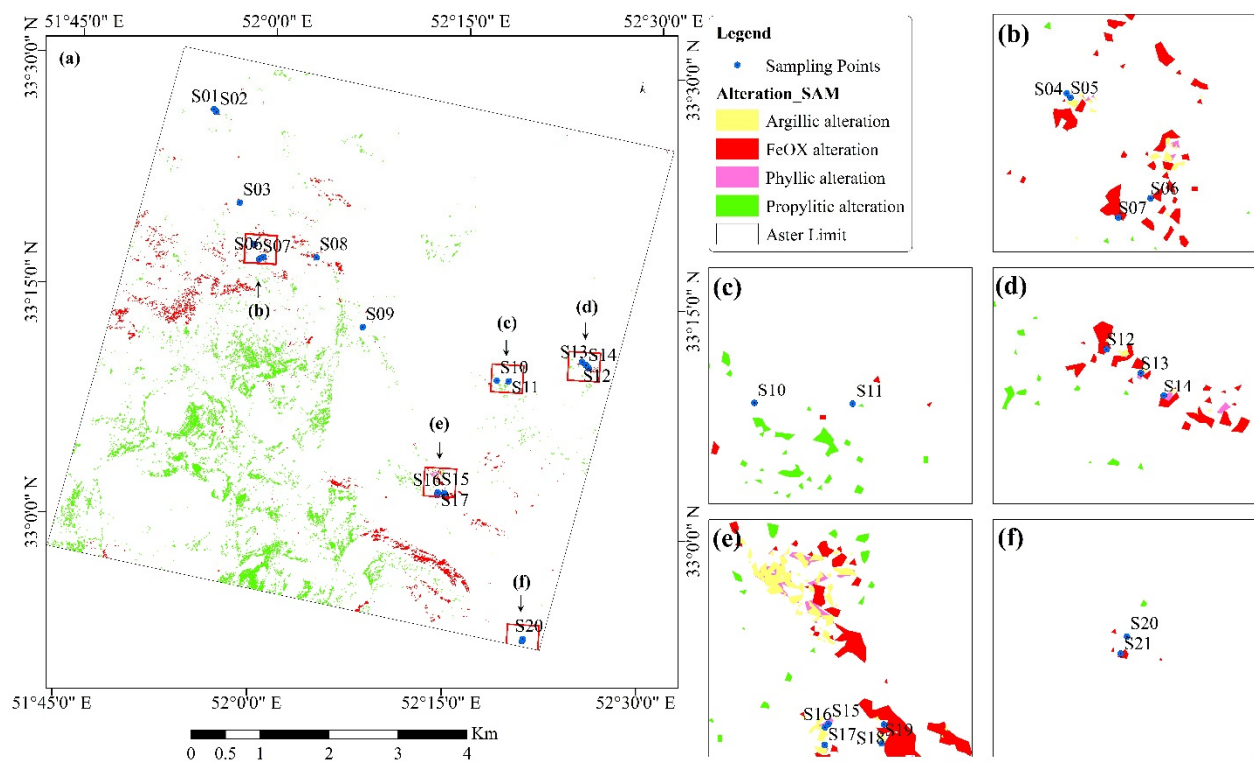


**Figure 10.** (a) The results of SAM spectral mapping on the ASTER data. (a) ASTER full scene of the study area. (b–f) Selected subsets for sampling and field survey.

The S01 and S02 samples were taken from the northwestern part of the study area. The rock of this area is diorite, which had been altered to argillic, phyllic, and iron oxides. The SVM results showed phyllic and argillic alteration, and the SAM method performed better in determining iron oxides in this area. The S03 was sampled from rhyodacite rocks. In this area, the rocks had been altered to sericite and silica. The zone of S04 and S05 sampling (Figure 11a) consisted of rhyolite and dacite rocks with calcareous interlayers altered to argillic and phyllic caused by intrusive masses. The S06 and S07 samples that were collected from marl and limestone tuffs had been severely altered by the intrusion of diorite and rhyodacite rocks. In this area, the thickness of the adjacent metamorphic zone, which consisted mainly of garnet and epidote, reached about 100 m. There were lenses made of silica and iron oxide with a thickness of 2 m among these skarns. The S08 sample was composed of rhyodacite and breccias tuff. This area incurred argillic alteration and is strongly siliceous along northwest-southeast faults. Sampling was performed from the S09 point owing to the presence of multiple faults and the detection of argillic alteration in the SVM results. During the field survey, a skarn mass was observed, and silicification and epidotization were identified in some parts of this zone. The S10 and S11 samples were taken from granodiorite and diorite, where argillic, advanced argillic, and propylitic alteration occurred. Mn dendrites were observed in this part. The S12, S13 and S14 samples were taken from the zones of argillic, propylitic, phyllic alterations and iron oxides (Figure 11b), which were identified in the SVM and SAM maps. At the field surveys, the argillic alteration was observed in a pyroclastic tuff unit, and in some parts the partial silicification alteration was recorded. The S15, S16, S17, S18 and S19 samples were taken from the southern part of the study area (Figure 11c). The field survey of these points showed that the porphyry dacites had been altered to argillic, phyllic, iron oxides, and silica. The S20 and S21 samples were collected from the southeastern part of the study area. This area is a pyroclastic complex that was influenced by dacite to diorite masses. Argillitization (Figure 11d), silicification, turmalinization, and iron oxides were seen in this zone.

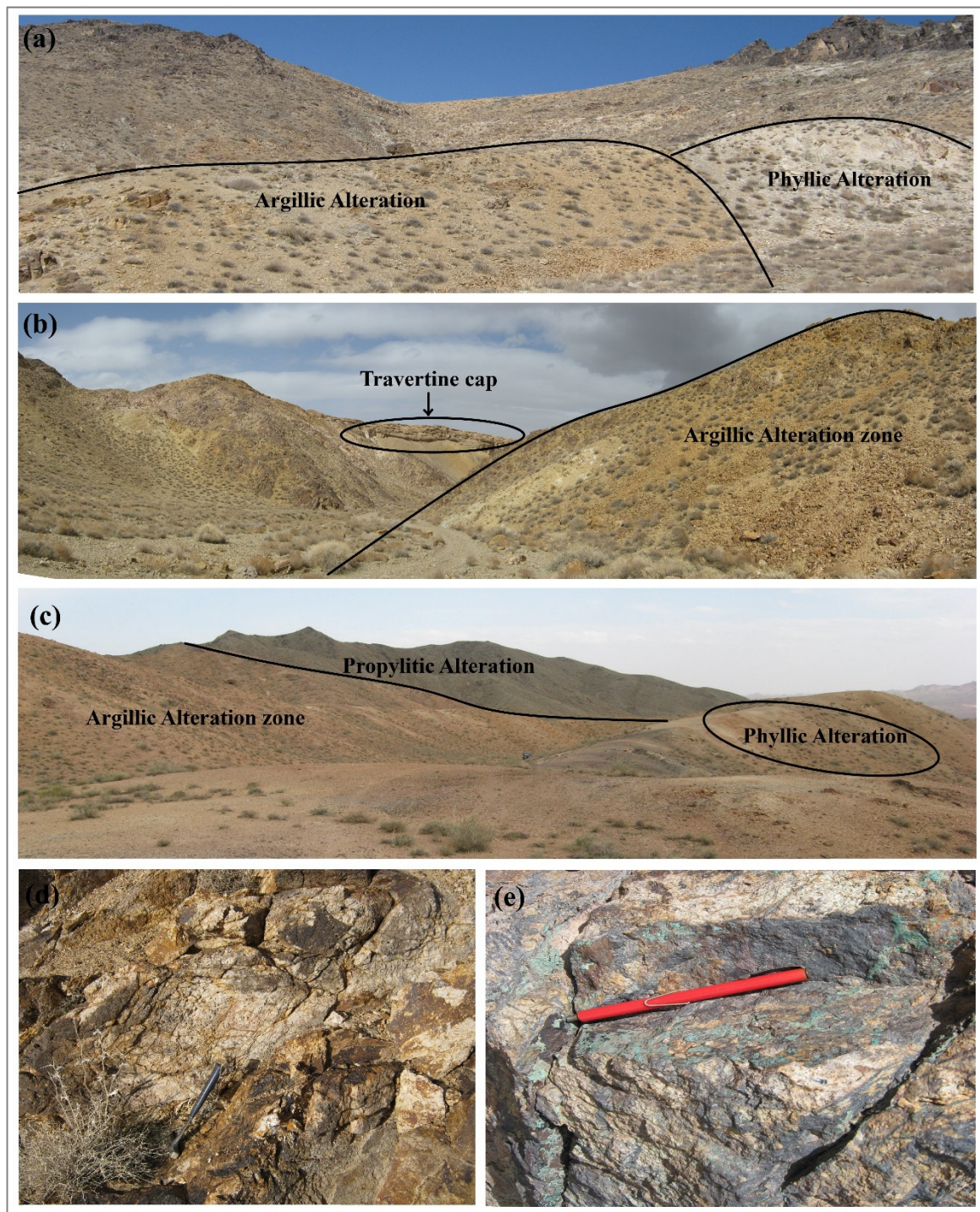


**Figure 11.** (a) Argillic and phyllic alterations in the area of the S04 and S05 sampling points; (b) argillic alteration in the area where the S12, S13 and S14 samples were taken; (c) propylitic, argillic and phyllic alteration in the S15, S16, S17, S18 and S19 sampling zones; (d) argillic alteration; (e) malachite mineralization observed in the southeastern part of the study area.

### 5.1. Petrography Study

The thin section in Figure 12a was prepared from the S04 sample. This thin section had a porphyry texture with a microgranular matrix. This sample had undergone pervasive alteration, and the rock had been entirely replaced by secondary minerals such as sericite, quartz, clay minerals, and iron oxides. Quartz veins were also observable. The thin section of the sample S07 (Figure 12b) was a porphyry rhyodacite with a hyalomicrogranular matrix. Rock feldspar minerals were selectively altered to sericite, illite, and muscovite.

Alteration to clay minerals, especially kaolinite, was observed throughout the thin section. Iron oxides were observed on the opaque minerals. In the thin section of the sample S13 rhyodacite porphyry with hyalomicrogranular matrix was detected (Figure 12c). Euhedral and subhedral plagioclase, alkaline feldspar, and quartz with corrosion gulf were the rock's main minerals. Tourmaline was also found among feldspar crystals. The main alterations observed in this section were argillic, sericite and phyllic. The thin section in Figure 12d was prepared from sample S19 corresponding to a lithic tuff with a volcanoclastic texture. Subhedral to amorphous plagioclase–alkali crystals, feldspar, and quartz were the main minerals, which had been altered to sericite, muscovite, iron oxides, and clay minerals.

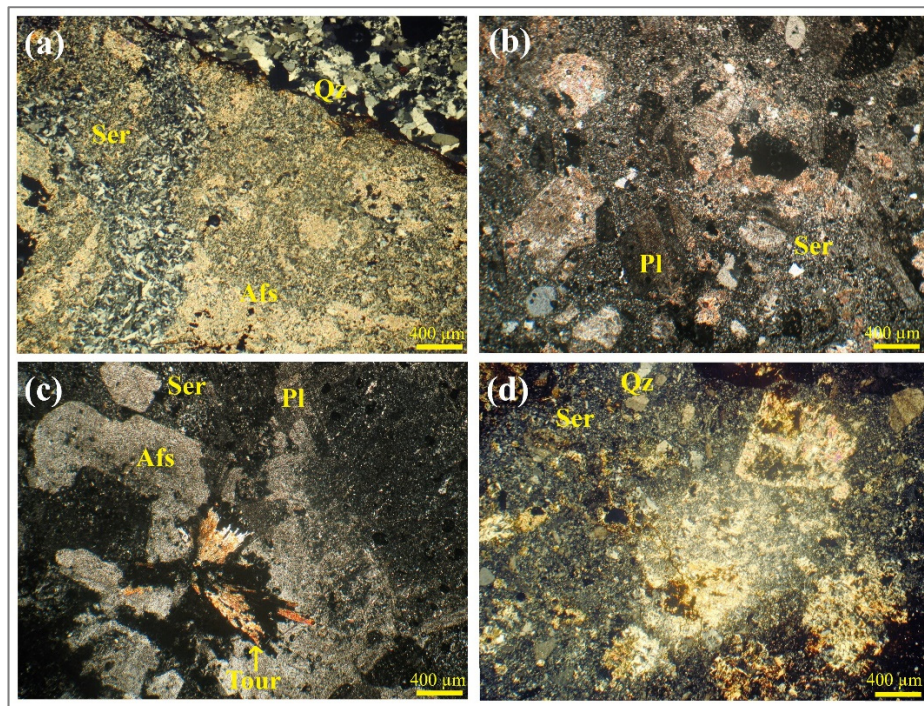


**Figure 12.** Thin sections of (a) the S04, (b) S07, (c) S13, and (d) S19 rock samples. The dusty surface of the images is due to the alteration and formation of clay and sericite minerals. Abbreviations: Ser = Sericite, and Qt = quartz, Afs = Alkali-feldspar, Pl = plagioclase, Tour = Tourmaline.

In the XRD results, indicator minerals for phyllic, argillic, and propylitic alteration zones such as hematite, muscovite, illite, kaolinite, montmorillonite, chlorite, epidote, and goethite were detected (Figure 13a–g and Appendix A, Table A3), which confirmed the results of the remote sensing analysis.

### 5.2. Geochemical Analysis

ICP-MS and XRF analyses were performed on all 21 samples taken from the study areas. The ICP-MS analysis of the S04 sample showed enrichment of Au (104 ppb), As (289 ppm), Cu (467 ppm), and Mo (21 ppm) elements (Appendix A, Table A1). In the ICP-MS results of S06 and S07 samples, the Zn enrichment (1195 and 3014 ppm) was observable (Appendix A, Table A1). In the S09 sample, Mn (3464 ppm), Cu (198 ppm) and Au (60 ppb) showed enrichment (Appendix A, Table A1). The ICP-MS results of the S11 sample analysis showed Mn (1664 ppm) enrichment (Appendix A, Table A1). Pb (280 ppm) and Cu (509 ppm) enrichment in the form of malachite were observed at the location of Figure 11e, from which the S21 sample was collected (Appendix A, Table A1). The XRF analysis was performed for all samples; the results are shown in Appendix A, Table A2. Altered samples showed high amounts of  $\text{Al}_2\text{O}_3$  (17.00% up to 24.20%),  $\text{SiO}_2$  (41.42% up to 56.24%), and  $\text{Fe}_2\text{O}_3$  (2.44 % up to 9.43%) and low amounts of  $\text{Na}_2\text{O}$  (<0.1% up to 3.68%) and  $\text{K}_2\text{O}$  (1.85% up to 3.70%) owing to alteration processes (Appendix A, Table A2).

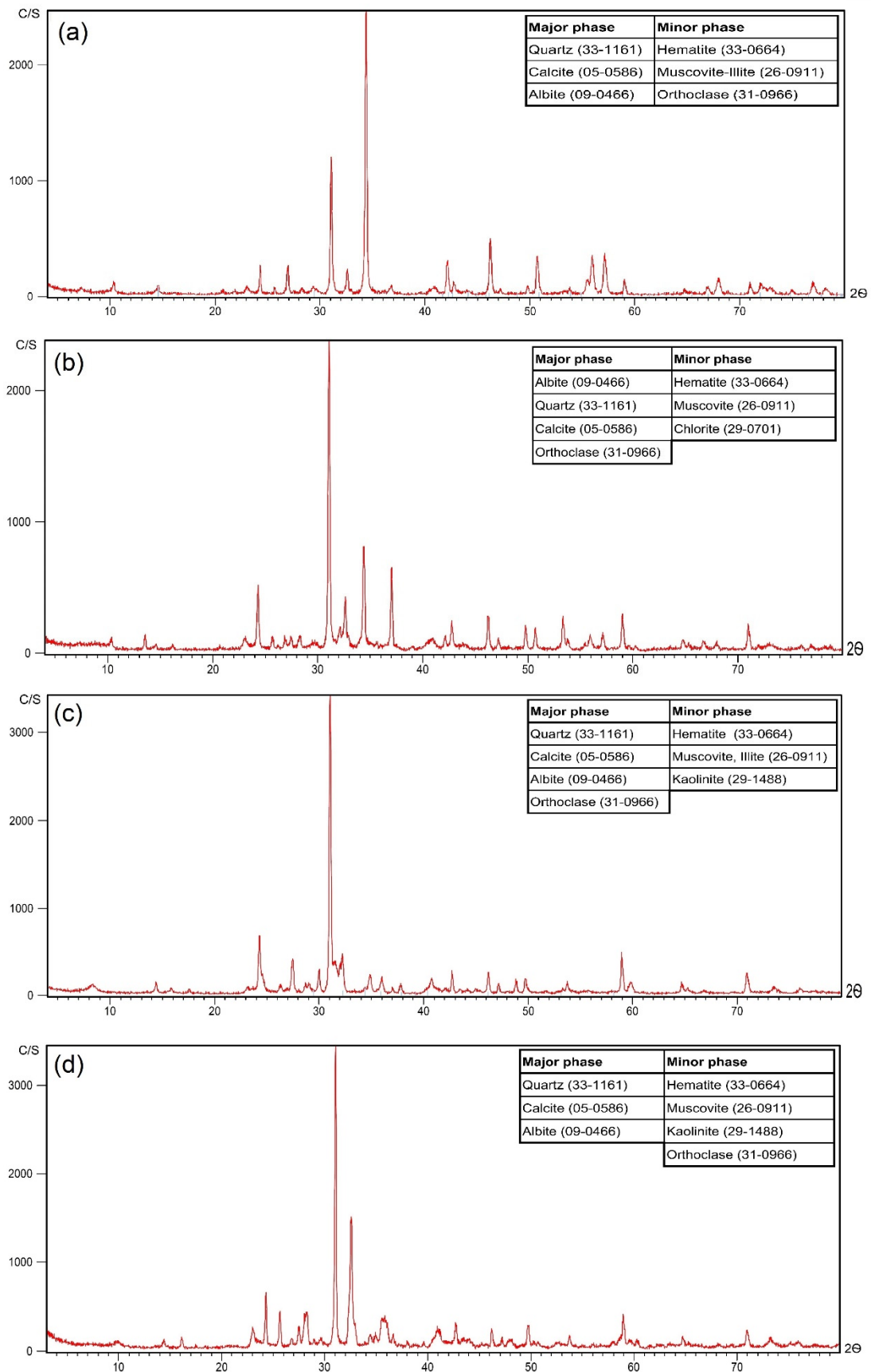
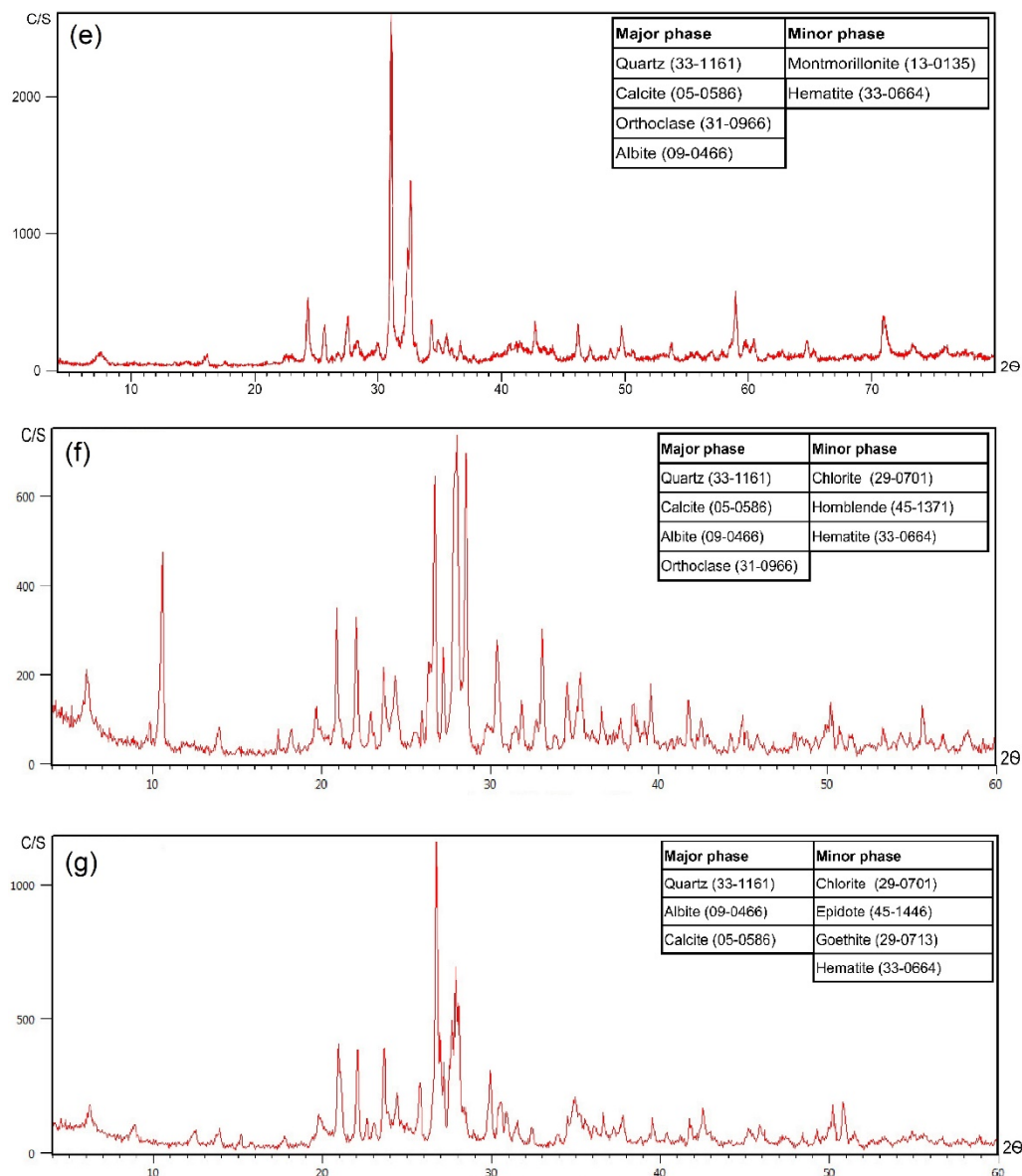


Figure 13. Cont.



**Figure 13.** The XRD analysis of (a) the S04, (b) S07, (c) S13, (d) S19, (e) S21, (f) S14, and (g) S16 samples. The XRD results of (a,b) show peaks of phyllic alteration. (c,d) show peaks of phyllic–argillic alteration minerals. The XRD in (e) shows argillic alteration. The peaks in (f,g) indicate that samples S14 and S16 were collected from propylitic alteration. The C/S means Count per second is y title and  $2\theta$  is the x title.

## 6. Accuracy Assessment

To evaluate the performances of the SVM and SAM methods, classification results were compared with the DP results. In this comparison, the DP results that included the alteration of phyllite, argillic, propylitic, and iron oxides were used as ground truth. User accuracy, producer accuracy, overall accuracy, and kappa coefficient [70,71] were calculated to evaluate the accuracy of the results. The results showed a total accuracy of 84.4 and 67.2% for SVM and SAM, respectively. The value of the kappa coefficient for SVM was 0.74 and for SAM it was 0.52. As can be seen from Tables 1 and 2, the classification of the phyllic, argillic, and propylitic alteration results of the SVM method were more accurate, but the Fe-oxides alteration result of the SAM classification was more consistent with ground truth. The best result was in the classification of propylitic alteration in the SVM method.

**Table 1.** Confusion matrix for the SVM classification.

Classes	Phyllic	Argillic	Propylitic	Fe-Oxides	Total	User's Accuracy
Unclassified	20	46	9	30	105	
Phyllic	172	23	0	0	195	88.21
Argillic	33	795	6	47	881	90.24
Propylitic	0	3	201	1	205	98.05
Fe-Oxides	0	17	0	104	121	85.95
Total	225	884	216	182	1507	
Producer's accuracy	76.44	89.93	93.06	57.14		
Overall accuracy	84.4					
Kappa coefficient	0.744					

**Table 2.** Confusion matrix for the SAM classification.

Classes	Phyllic	Argillic	Propylitic	Fe-Oxides	Total	User's Accuracy
Unclassified	8	102	47	23	180	
Phyllic	146	107	0	7	260	56.15
Argillic	43	586	0	15	644	90.99
Propylitic	0	1	128	0	129	99.22
Fe-Oxides	24	108	9	153	294	52.04
Total	221	904	184	198	1507	
Producer's accuracy	66.06	64.82	69.57	77.27		
Overall accuracy	67.2					
Kappa coefficient	0.52					

## 7. Discussion

Distinguishing hydrothermal alteration zones resulting from hydrothermal processes in the porphyry systems is a significant stage of mineral exploration [58]. Remote sensing data have a great capability for mapping hydrothermal alteration zones and are extensively and successfully used for distinguishing hydrothermal alteration minerals and zones in metallogenic provinces around the world [8,9,72–74]. Several image processing techniques are broadly applied to remote sensing imagery for classifying, identifying, and distinguishing spatial distribution of alteration minerals and zones [61,62]. Band ratios, Principal Component Analysis (PCA), Independent Component Analysis (ICA), Matched-Filtering (MF), Mixture-Tuned Matched-Filtering (MTMF), Linear Spectral Mixing (LUS), and Constrained Energy Minimization (CEM) methods have been extensively implemented on ASTER data for mapping alteration zones associated with porphyry copper deposits [75–77]. However, these techniques are conceptual (i.e., knowledge-driven) algorithms and the reconfiguration formula is used to map the desired criteria. Consequently, the zones that encounter most of the desired criteria are highlighted as prospective zones. These algorithms are provisional regarding the type of input remote sensing data and thus can be biased. By applying these algorithms, expert knowledge is used more than the proficiency of the statistical methods [78]. The application of ML algorithms to remote sensing data has high potential to produce accurate maps, especially for mapping argillic, phyllic, and propylitic zones associated with porphyry copper deposits [78–80].

In hydrothermal alteration mapping, the placement of each pixel in a cluster is essential. Hence, the image processing methods categorizing only a fraction of the pixels into a particular class are not very effective and accurate. In view of that, the use of clustering methods is highly useful in determining the ML of a pixel belonging to a cluster. This study showed that the fusion of unsupervised and supervised methods in mineral mapping leads to more accurate results. The methods and algorithms used for mineral mapping are in line with the reality of the data and provide better results. The DP method used in this study models alteration zones well because its performance is based on distribution. Consequently, in specifying training data, it is more consistent with reality than using

endmembers or pure training data. More reliable results can be obtained especially when the detection methods are used to determine the extent of each alteration zone. The training data achieved from the DP method are suitable input for use in the SVM and SAM methods. The SVM method with RBF kernel and training data generated from the DP showed better results than SAM. Furthermore, the DP method can also be used to cluster all other types of data, including the results of geochemical analysis of stream sediments, lithochemical and geophysical data, etc., which can be applied in the future mineral exploration in metallogenic provinces.

Geological surveys were performed based on the results obtained from remote sensing imagery. The results of the fieldwork and laboratory analysis showed good accordance with the obtained remote sensing results. The presence of illite and muscovite minerals in the XRD results indicated a phyllic alteration zone in the study area. The occurrence of kaolinite and montmorillonite minerals in the XRD results confirmed the occurrence of an argillic alteration zone in the study areas. The manifestation of epidote and chlorite minerals in the XRD results indicated a propylitic alteration. In the XRF results, owing to the degradation of feldspars in the alteration process, the amounts of  $K_2O$ ,  $CaO$ , and  $Na_2O$  decreased and the  $Al_2O_3$ ,  $Fe_2O_3$ , and  $SiO_2$  increased. Increasing the amount of Cu, Au, Zn, and Mn obtained in the ICP-MS results was related to copper mineralization in some samples collected from different zones in the study area. Consequently, the remote sensing approach applied in this study was a valuable tool for porphyry copper exploration in the metallogenic provinces.

## 8. Conclusions

Mineral mapping using supervised methods requires appropriate training data to classify the data accurately and comprehensively. Considering that minerals and rocks have various compositions, the DP method was used to model phyllic, argillic, propylitic, and Fe-oxides alteration zones in the Zefreh porphyry copper deposits. The classification maps with the DP results training data were more accurate. The DP process was used to specify the training data on ASTER images of the Zefreh porphyry copper deposits, where alteration zones were detected by spectral mapping methods such as BDR, LSU, OSP, and SFF. The DP clustering results were realistic, considering the field survey and laboratory analysis. By performing the SVM and SAM methods on the ASTER data, areas including phyllic, argillic, propylitic, and iron oxide alterations in the full ASTER scene were identified. By field survey of these zones, a good coincidence was perceived between the results obtained from the SVM method and field observations. Alteration zones similar to those obtained from the SVM results were observed in the field at most of the surveyed points. With the SAM method, most of the iron oxides and propylitic alterations were identified, and in some areas, it was less compatible with the alterations observed in the field than the SVM method. This study reinforced the application of the SVM algorithm for mapping hydrothermal alteration zones associated with porphyry copper deposits, which is applicable to ASTER data for potential mapping in various metallogenic provinces around the world.

**Author Contributions:** Conceptualization, M.Y. and S.H.T.; methodology, M.Y. and A.B.P.; software, M.Y. and R.R.; validation, M.Y.; data curation, M.Y. and S.H.T.; writing—original draft preparation M.Y.; writing—review and editing, A.B.P.; supervision, S.H.T. and B.P.; fieldwork, M.Y. and S.H.T. All authors have read and agreed to the published version of the manuscript.

**Funding:** The present work has received no funding or grant.

**Data Availability Statement:** The data presented in this study are available on request from the corresponding author.

**Acknowledgments:** The authors' thanks are also extended to the Board of Directors of Parsi Kan Kav Company for providing some information on the study areas.

**Conflicts of Interest:** The authors declare no conflict of interest.

## Appendix A

**Table A1.** ICP-MS analysis results of some significant elements (Au unit: part per billion, other element unit: part per million).

Row	Sample_NO	X (m)	Y (m)	Au (ppb)	Fe	Ag	As	Cu	Mn	Mo	Pb	Sb	Zn
1	S01	585,770	3,701,063	<5	5855	0	8.3	18	178	2.1	5	1.08	20
2	S02	586,064	3,700,766	<5	17,302	0	8.9	5	29	5.3	5	1.24	53
3	S03	589,488	3,690,065	70	13,866	0	150.7	15	219	6.8	63	201	39
4	S04	591,489	3,685,219	104	185,397	0	289.2	467	161	20.9	86	1.1	138
5	S05	591,544	3,685,158	<5	21,278	0	9.1	6	67	2.18	6	1.29	16
6	S06	592,703	3,683,705	7	123,344	0	8.9	112	564	4.8	32	1.09	1195
7	S07	592,237	3,683,423	<5	14,281	0	909.2	346	10,111	7.4	124	1.26	3014
8	S08	599,089	3,684,040	<5	8571	0.27	16.2	6	59	4	7	1.02	9
9	S09	605,129	3,675,998	60	81,444	0.35	28.1	198	3464	2.27	32	1.17	60
10	S10	621,599	3,670,515	<5	35,705	0.27	8.8	16	110	3.4	7	1.13	78
11	S11	623,023	3,670,502	<5	47,093	0.22	8.9	63	1664	2.31	37	1.09	234
12	S12	631,737	3,673,323	<5	15,726	0.24	11.2	28	65	2.43	7	1.12	18
13	S13	632,235	3,672,977	<5	27,364	0.28	8.4	40	49	3.2	197	1.02	119
14	S14	632,566	3,672,641	8	77,478	0.36	36.4	12	80	26.9	25	1.06	23
15	S15	615,304	3,656,553	12	37,739	0.22	8.6	8	29	2.16	5	1.01	22
16	S16	615,253	3,656,502	23	20,271	0.25	8.3	40	48	6.6	5	0.97	19
17	S17	615,249	3,656,248	25	42,181	0.27	120.8	10	39	2.27	13	1.09	22
18	S18	616,106	3,656,542	6	17,893	0.28	8.4	24	52	3.8	6	1.02	17
19	S19	616,073	3,656,271	<5	43,412	0.22	8.8	56	115	2.1	7	1.1	37
20	S20	626,512	3,639,545	<5	18,158	0	13	29	36	8.1	9	1.05	6
21	S21	626,422	3,639,297	55	39,771	0	61.7	509	63	9.6	280	1.04	16

**Table A2.** XRF analysis results of some main oxides (Oxides unit: percent). L.O.I: Loss Of Ignition.

Row	Sample_NO	SiO <sub>2</sub>	Al <sub>2</sub> O <sub>3</sub>	CaO	MgO	TiO <sub>2</sub>	Fe <sub>2</sub> O <sub>3</sub>	MnO	P <sub>2</sub> O <sub>5</sub>	Na <sub>2</sub> O	K <sub>2</sub> O	SrO	L.O.I	Total
1	S01	56.24	24.19	0.71	0.66	0.75	3.14	<0.1	0.48	<0.1	2.24	<0.1	10.70	99.11
2	S02	49.23	22.81	2.70	1.55	0.85	6.08	0.14	0.46	1.54	3.23	<0.1	10.00	98.60
3	S03	41.85	20.15	8.97	2.94	0.61	6.81	0.28	0.38	0.32	2.23	<0.1	13.50	98.04
4	S04	50.16	23.24	5.66	1.58	0.43	3.43	<0.1	0.32	<0.1	1.94	<0.1	11.30	98.06
5	S05	47.91	23.51	6.90	1.64	0.43	4.01	<0.1	0.34	<0.1	2.81	<0.1	11.49	99.03
6	S06	43.86	22.51	6.31	1.39	0.65	7.35	0.17	0.31	0.62	2.91	<0.1	12.62	98.70
7	S07	53.06	18.94	4.31	3.26	0.71	6.49	0.26	0.42	3.68	3.58	<0.1	4.14	98.85
8	S08	43.38	18.91	8.87	2.86	0.66	6.80	0.16	0.43	1.99	2.22	0.12	12.70	99.08
9	S09	52.32	22.22	5.02	2.14	0.50	2.44	<0.1	0.34	<0.1	3.85	<0.1	9.50	98.33
10	S10	41.42	17.01	8.66	3.44	0.77	9.28	0.33	0.57	2.56	1.85	0.10	12.98	98.98
11	S11	44.85	21.87	4.79	2.21	0.62	7.67	0.15	0.36	0.65	3.27	<0.1	12.34	98.77
12	S12	49.31	19.29	5.46	2.63	0.55	6.14	0.15	0.38	2.33	2.46	<0.1	9.39	98.09
13	S13	48.28	17.41	8.81	3.28	0.69	8.44	0.18	0.52	2.97	3.62	0.19	5.15	99.56
14	S14	44.26	17.00	6.57	3.07	0.75	8.95	0.17	0.37	2.91	3.70	0.10	9.84	97.69
15	S15	56.24	24.19	0.71	0.66	0.75	3.14	<0.1	0.48	<0.1	2.24	<0.1	6.70	95.11
16	S16	49.23	22.81	2.70	1.55	0.85	6.08	0.14	0.46	1.54	3.23	<0.1	10.00	98.60
17	S17	41.85	20.15	8.97	2.94	0.61	6.81	0.28	0.38	0.32	2.23	<0.1	13.50	98.04
18	S18	50.16	23.24	5.66	1.58	0.43	3.43	<0.1	0.32	<0.1	1.94	<0.1	11.30	98.06
19	S19	47.91	23.51	6.90	1.64	0.43	4.01	<0.1	0.34	<0.1	2.81	<0.1	11.49	99.03
20	S20	43.86	22.51	6.31	1.39	0.65	7.35	0.17	0.31	0.62	2.91	<0.1	12.62	98.70
21	S21	53.06	18.94	4.31	3.26	0.71	6.49	0.26	0.42	3.68	3.58	<0.1	4.14	98.85

**Table A3.** The results of the XRD analysis.

Samples	Major Phase	Minor Phase	Alteration
S04 S07	Quartz, Calcite, Albite Albite, Quartz, Calcite, Orthoclase	Hematite, Muscovite, Illite, Orthoclase Hematite, Muscovite, Chlorite	Phyllic Phyllic
S13 S19	Quartz, Calcite, Albite, Orthoclase Quartz, Calcite, Albite	Hematite, Muscovite, Illite, Kaolinite Hematite, Muscovite, Kaolinite, Orthoclase	Phyllic–Argillic Phyllic–Argillic
S21	Quartz, Calcite, Orthoclase, Albite	Montmorillonite, Hematite	Argillic
S14 S16	Quartz, Calcite, Albite, Orthoclase Quartz, Albite, Calcite	Chlorite, Hornblende, Hematite Chlorite, Epidote, Goethite, Hematite	Propylitic Propylitic

## References

1. El-Wahed, M.A.; Zoheir, B.; Pour, A.B.; Kamh, S. Shear-Related Gold Ores in the Wadi Hodein Shear Belt, South Eastern Desert of Egypt: Analysis of Remote Sensing, Field and Structural Data. *Minerals* **2021**, *11*, 474. [\[CrossRef\]](#)
2. Krupnik, D.; Khan, S.D. High-Resolution Hyperspectral Mineral Mapping: Case Studies in the Edwards Limestone, Texas, USA and Sulfide-Rich Quartz Veins from the Ladakh Batholith, Northern Pakistan. *Minerals* **2020**, *10*, 967. [\[CrossRef\]](#)
3. Ghezalbash, R.; Maghsoudi, A.; Carranza, E.J.M. Performance evaluation of RBF-and SVM-based machine learning algorithms for predictive mineral prospectivity modeling: Integration of SA multifractal model and mineralization controls. *Earth Sci. Inform.* **2019**, *12*, 277–293. [\[CrossRef\]](#)
4. Cardoso-Fernandes, J.; Teodoro, A.C.; Lima, A.; Perrotta, M.; Roda-Robles, E. Detecting Lithium (Li) mineralizations from space: Current research and future perspectives. *Appl. Sci.* **2020**, *10*, 1785. [\[CrossRef\]](#)
5. Peyghambari, S.; Zhang, Y. Hyperspectral remote sensing in lithological mapping, mineral exploration, and environmental geology: An updated review. *J. Appl. Remote Sens.* **2021**, *15*, 031501. [\[CrossRef\]](#)
6. Hewson, R.; Mshiu, E.; Hecker, C.; van der Werff, H.; van Ruitenbeek, F.; Alkema, D.; van der Meer, F. The application of day and night time ASTER satellite imagery for geothermal and mineral mapping in East Africa. *IJAEO* **2020**, *85*, 101991. [\[CrossRef\]](#)
7. Adiri, Z.; Lhissou, R.; El Harti, A.; Jellouli, A.; Chakouri, M. Recent advances in the use of public domain satellite imagery for mineral exploration: A review of Landsat-8 and Sentinel-2 applications. *Ore Geol. Rev.* **2020**, *117*, 103332. [\[CrossRef\]](#)
8. Pour, A.B.; Hashim, M.; Hong, J.K.; Park, Y. Lithological and alteration mineral mapping in poorly exposed lithologies using Landsat-8 and ASTER satellite data: North-eastern Graham Land, Antarctic Peninsula. *Ore Geol. Rev.* **2019**, *108*, 112–133. [\[CrossRef\]](#)
9. Pour, A.B.; Zoheir, B.; Pradhan, B.; Hashim, M. Editorial for the Special Issue: Multispectral and Hyperspectral Remote Sensing Data for Mineral Exploration and Environmental Monitoring of Mined Areas. *Remote Sens.* **2021**, *13*, 519. [\[CrossRef\]](#)
10. Gupta, P.; Venkatesan, M. Mineral identification using unsupervised classification from hyperspectral data. In *Emerging Research in Data Engineering Systems and Computer Communications*; Springer: Berlin/Heidelberg, Germany, 2020; pp. 259–268.
11. Pour, A.B.; Park, T.-Y.S.; Park, Y.; Hong, J.K.; Zoheir, B.; Pradhan, B.; Ayoobi, I.; Hashim, M. Application of multi-sensor satellite data for exploration of Zn–Pb sulfide mineralization in the Franklinian Basin, North Greenland. *Remote Sens.* **2018**, *10*, 1186. [\[CrossRef\]](#)
12. Wylie, B.K.; Pastick, N.J.; Picotte, J.J.; Deering, C.A. Geospatial data mining for digital raster mapping. *GISci. Remote Sens.* **2019**, *56*, 406–429. [\[CrossRef\]](#)
13. Dhingra, S.; Kumar, D. A review of remotely sensed satellite image classification. *Int. J. Electr. Comput. Eng.* **2019**, *9*, 1720–1731. [\[CrossRef\]](#)
14. Gemusse, U.; Lima, A.; Teodoro, A. Comparing different techniques of satellite imagery classification to mineral mapping pegmatite of Muiane and Naipa: Mozambique. In *Proceedings of the Earth Resources and Environmental Remote Sensing/GIS Applications X*, Strasbourg, France, 10–12 September 2019; p. 111561E.
15. Bachri, I.; Hakdaoui, M.; Raji, M.; Teodoro, A.C.; Benbouziane, A. Machine learning algorithms for automatic lithological mapping using remote sensing data: A case study from Souk Arbaa Sahel, Sidi Ifni Inlier, Western Anti-Atlas, Morocco. *ISPRS Int. J. Geo-Inf.* **2019**, *8*, 248. [\[CrossRef\]](#)
16. Mojeddifar, S.; Mavadati, M. Integration of support vector machines for hydrothermal alteration mapping using ASTER data—case study: The northwestern part of the Kerman Cenozoic Magmatic Arc, Iran. *Int. J. Min. Geo-Eng.* **2020**, *54*, 45–50.
17. Cardoso-Fernandes, J.; Teodoro, A.C.; Lima, A.; Roda-Robles, E. Semi-automatization of support vector machines to map lithium (Li) bearing pegmatites. *Remote Sens.* **2020**, *12*, 2319. [\[CrossRef\]](#)
18. Reddy, C.K. *Data Clustering: Algorithms and Applications*; Chapman and Hall/CRC: London, UK, 2018.
19. Abdi Jalebi, S.; Sharifzadeh, S.; Amiri, S. A New Method for Semi-Supervised Segmentation of Satellite Images. In *Proceedings of the 2021 22nd IEEE International Conference on Industrial Technology (ICIT)*, Valencia, Spain, 10–12 March 2021; IEEE: New York, NY, USA, 2021.
20. Saxena, A.; Prasad, M.; Gupta, A.; Bharill, N.; Patel, O.P.; Tiwari, A.; Er, M.J.; Ding, W.; Lin, C.-T. A review of clustering techniques and developments. *Neurocomputing* **2017**, *267*, 664–681. [\[CrossRef\]](#)
21. Yang, M.-S.; Sinaga, K.P. A feature-reduction multi-view k-means clustering algorithm. *IEEE Access* **2019**, *7*, 114472–114486. [\[CrossRef\]](#)
22. Ünlü, R.; Xanthopoulos, P. Estimating the number of clusters in a dataset via consensus clustering. *Expert Syst. Appl.* **2019**, *125*, 33–39. [\[CrossRef\]](#)
23. Khosravi, M.; Rajabzadeh, M.A.; Qin, K.; Asadi, H.H. Tectonic setting and mineralization potential of the Zefreh porphyry Cu–Mo deposit, central Iran: Constraints from petrographic and geochemical data. *J. Geochem. Explor.* **2019**, *199*, 1–15. [\[CrossRef\]](#)
24. Khosravi, M.; Christiansen, E.H.; Rajabzadeh, M.A. Chemistry of rock-forming silicate and sulfide minerals in the granitoids and volcanic rocks of the Zefreh porphyry Cu–Mo deposit, central Iran: Implications for crystallization, alteration, and mineralization potential. *Ore Geol. Rev.* **2021**, *124*, 104150. [\[CrossRef\]](#)
25. Salehi, T.; Tangestani, M.H. Large-scale mapping of iron oxide and hydroxide minerals of Zefreh porphyry copper deposit, using Worldview-3 VNIR data in the Northeastern Isfahan, Iran. *IJAEO* **2018**, *73*, 156–169. [\[CrossRef\]](#)
26. Abrams, M. The Advanced Spaceborne Thermal Emission and Reflection Radiometer (ASTER): Data products for the high spatial resolution imager on NASA's Terra platform. *IJRS* **2000**, *21*, 847–859. [\[CrossRef\]](#)

27. Guo, Y.-D.; Shi, Z. Characteristics and Applications of ASTER. *Remote Sens. Technol. Appl.* **2003**, *5*, 346–352.
28. Erenoglu, R.C.; Arslan, N.; Erenoglu, O.; Arslan, E. Application of spectral analysis to determine geothermal anomalies in the Tuzla region, NW Turkey. *Arab. J. Geosci.* **2019**, *12*, 1–15. [[CrossRef](#)]
29. Shawkya, M. Comparative Study of Atmospheric Correction Methods of ASTER Data to Enhance the Delineation of Uranium Mineralized Zones. *Int. J. Intell. Comput. Inf. Sci.* **2019**, *19*, 48–65. [[CrossRef](#)]
30. Tucker, C.J. Red and photographic infrared linear combinations for monitoring vegetation. *Remote Sens. Environ.* **1979**, *8*, 127–150. [[CrossRef](#)]
31. Ferguson, T.S. A Bayesian analysis of some nonparametric problems. *Ann. Stat.* **1973**, *1*, 209–230. [[CrossRef](#)]
32. Escobar, M.D.; West, M. Bayesian density estimation and inference using mixtures. *J. Am. Stat. Assoc.* **1995**, *90*, 577–588. [[CrossRef](#)]
33. Duan, J.A.; Guindani, M.; Gelfand, A.E. Generalized spatial Dirichlet process models. *Biometrika* **2007**, *94*, 809–825. [[CrossRef](#)]
34. Ma, Z.; Lai, Y.; Kleijn, W.B.; Song, Y.-Z.; Wang, L.; Guo, J. Variational Bayesian learning for Dirichlet process mixture of inverted Dirichlet distributions in non-Gaussian image feature modeling. *IEEE Trans. Neural Netw. Learn. Syst.* **2018**, *30*, 449–463. [[CrossRef](#)]
35. Teh, Y.W.; Jordan, M.I.; Beal, M.J.; Blei, D.M. Sharing clusters among related groups: Hierarchical Dirichlet processes. *Adv. Neural Inf. Process. Syst.* **2005**, *17*, 1385–1392.
36. Vlachos, A.; Ghahramani, Z.; Korhonen, A. Dirichlet process mixture models for verb clustering. In Proceedings of the ICML Workshop on Prior Knowledge for Text and Language, Helsinki, Finland, 9 July 2008.
37. Lugrin, T. *Bayesian Semiparametrics for Modelling the Clustering of Extreme Values*; École polytechnique fédérale de Lausanne: Écublens, Switzerland, 2013.
38. Jain, A.; Murty, M.; Flynn, P.J. Data clustering: A review. *ACM Comput. Surv.* **2011**, *31*, 264–323. [[CrossRef](#)]
39. Zuo, R.; Carranza, E.J.M. Support vector machine: A tool for mapping mineral prospectivity. *Comput. Geosci.* **2011**, *37*, 1967–1975. [[CrossRef](#)]
40. Wang, K.; Cheng, L.; Yong, B. Spectral-similarity-based kernel of SVM for hyperspectral image classification. *Remote Sens.* **2020**, *12*, 2154. [[CrossRef](#)]
41. Vapnik, V. *The Nature of Statistical Learning Theory*; Springer: New York, NY, USA, 1995; pp. 841–842.
42. Ben-Hur, A.; Horn, D.; Siegelmann, H.T.; Vapnik, V. Support vector clustering. *J. Mach. Learn. Res.* **2001**, *2*, 125–137. [[CrossRef](#)]
43. Bennett, K.; Demiriz, A. Semi-Supervised Support Vector Machines. Available online: <https://proceedings.neurips.cc/paper/1998/file/b710915795b9e9c02cf10d6d2bdb688c-Paper.pdf> (accessed on 24 March 2021).
44. Widodo, A.; Yang, B.-S. Support vector machine in machine condition monitoring and fault diagnosis. *MSSP* **2007**, *21*, 2560–2574. [[CrossRef](#)]
45. Wainer, J.; Fonseca, P. How to tune the RBF SVM hyperparameters? An empirical evaluation of 18 search algorithms. *Artif. Intell. Rev.* **2021**, *54*, 4771–4797. [[CrossRef](#)]
46. Morales, R.; Wang, Y.; Zhang, Z. Unstructured point cloud surface denoising and decimation using distance RBF K-nearest neighbor kernel. In Proceedings of the Pacific-Rim Conference on Multimedia, Shanghai, China, 21–24 September 2010; pp. 214–225.
47. Saljoughi, B.S.; Hezarkhani, A. A comparative analysis of artificial neural network (ANN), wavelet neural network (WNN), and support vector machine (SVM) data-driven models to mineral potential mapping for copper mineralizations in the Shahr-e-Babak region, Kerman, Iran. *Appl. Geomat.* **2018**, *10*, 229–256. [[CrossRef](#)]
48. Khaleghi, M.; Ranjbar, H.; Shahabpour, J.; Honarmand, M. Spectral angle mapping, spectral information divergence, and principal component analysis of the ASTER SWIR data for exploration of porphyry copper mineralization in the Sarduiyeh area, Kerman province, Iran. *Appl. Geomat.* **2014**, *6*, 49–58. [[CrossRef](#)]
49. Wang, M.; Huang, Z.; Zhang, X.; Zhang, Y.; Chen, M. Altered mineral mapping based on ground-airborne hyperspectral data and wavelet spectral angle mapper tri-training model: Case studies from Dehua-Youxi-Yongtai Ore District, Central Fujian, China. *IJAEO* **2021**, *102*, 102409.
50. Choi, J.; Kim, G.; Park, N.; Park, H.; Choi, S. A hybrid pansharpening algorithm of VHR satellite images that employs injection gains based on NDVI to reduce computational costs. *Remote Sens.* **2017**, *9*, 976. [[CrossRef](#)]
51. Renza, D.; Martinez, E.; Molina, I.J.A.i.S.R. Unsupervised change detection in a particular vegetation land cover type using spectral angle mapper. *AdSpR* **2017**, *59*, 2019–2031. [[CrossRef](#)]
52. Wolf, R.E.; Adams, M. *Multi-Elemental Analysis of Aqueous Geochemical Samples by Quadrupole Inductively Coupled Plasma-Mass Spectrometry (ICP-MS)*; US Department of the Interior, US Geological Survey: Washington, DC, USA, 2015.
53. Monecke, T.; Köhler, S.; Kleeberg, R.; Herzig, P.M.; Gemmel, J.B. Quantitative phase-analysis by the Rietveld method using X-ray powder-diffraction data: Application to the study of alteration halos associated with volcanic-rock-hosted massive sulfide deposits. *Can. Mineral.* **2001**, *39*, 1617–1633. [[CrossRef](#)]
54. Raith, M.M.; Raase, P. Thin Section Microscopy: A Comprehensive Guide. Available online: <http://nationalpetrographic.com/thin-section-microscopy-a-comprehensive-guide.html> (accessed on 24 March 2021).
55. Pichler, H.; Schmitt-Riegraf, C. *Rock-Forming Minerals in Thin Section*; Springer Science & Business Media: Berlin, Germany, 1997.
56. Chauhan, A.; Chauhan, P. Powder XRD technique and its applications in science and technology. *J. Anal. Bioanal. Tech.* **2014**, *5*, 1–5. [[CrossRef](#)]
57. Rajendran, S.; Nasir, S. Characterization of ASTER spectral bands for mapping of alteration zones of volcanogenic massive sulphide deposits. *Ore Geol. Rev.* **2017**, *88*, 317–335. [[CrossRef](#)]

58. Jain, R.; Sharma, R.U. Mapping of Mineral Zones using the Spectral Feature Fitting Method in Jahazpur belt, Rajasthan, India. *Int. Res. J. Eng. Technol. (IRJET)* **2018**, *5*, 562–567.
59. Zoheir, B.; Emam, A.; Abdel-Wahed, M.; Soliman, N. Multispectral and radar data for the setting of gold mineralization in the South Eastern Desert, Egypt. *Remote Sens.* **2019**, *11*, 1450. [[CrossRef](#)]
60. Chang, C.-I.; Cao, H.; Chen, S.; Shang, X.; Yu, C.; Song, M. Orthogonal subspace projection-based go-decomposition approach to finding low-rank and sparsity matrices for hyperspectral anomaly detection. *ITGRS* **2020**, *59*, 2403–2429. [[CrossRef](#)]
61. Pour, A.B.; Hashim, M. Identification of hydrothermal alteration minerals for exploring of porphyry copper deposit using ASTER data, SE Iran. *JAESc* **2011**, *42*, 1309–1323. [[CrossRef](#)]
62. Moghtaderi, A.; Moore, F.; Ranjbar, H. Application of ASTER and Landsat 8 imagery data and mathematical evaluation method in detecting iron minerals contamination in the Chadormalu iron mine area, central Iran. *J. Appl. Remote Sens.* **2017**, *11*, 016027. [[CrossRef](#)]
63. Kokaly, R.; Clark, R.; Swayze, G.; Livo, K.; Hoefen, T.; Pearson, N.; Wise, R.; Benzel, W.; Lowers, H.; Driscoll, R. *Usgs Spectral Library Version 7 Data: Us Geological Survey Data Release*; United States Geological Survey (USGS): Reston, VA, USA, 2017.
64. Sabins, F.F. Remote sensing for mineral exploration. *Ore Geol. Rev.* **1999**, *14*, 157–183. [[CrossRef](#)]
65. Pour, A.B.; Sekandari, M.; Rahmani, O.; Crispini, L.; Läufer, A.; Park, Y.; Hong, J.K.; Pradhan, B.; Hashim, M.; Hossain, M.S. Identification of phyllosilicates in the antarctic environment using aster satellite data: Case study from the Mesa range, Campbell and Priestley glaciers, northern Victoria Land. *Remote Sens.* **2021**, *13*, 38. [[CrossRef](#)]
66. Harsanyi, J.C.; Chang, C.-I. Hyperspectral image classification and dimensionality reduction: An orthogonal subspace projection approach. *ITGRS* **1994**, *32*, 779–785. [[CrossRef](#)]
67. Gelfand, A.E.; Smith, A.F. Sampling-based approaches to calculating marginal densities. *J. Am. Stat. Assoc.* **1990**, *85*, 398–409. [[CrossRef](#)]
68. Spiegelhalter, D.; Thomas, A.; Best, N.; Gilks, W. *Bayesian Inference Using Gibbs Sampling Manual (Version ii) BUGS 0.5*; MRC Biostatistics Unit, Institute of Public Health: Cambridge, UK, 1996; p. 59.
69. Spiegelhalter, D.; Thomas, A.; Best, N.; Lunn, D. WinBUGS User Manual. 2003. Available online: <https://www.mrc-bsu.cam.ac.uk/wp-content/uploads/manual14.pdf> (accessed on 27 February 2021).
70. Foody, G.M. Explaining the unsuitability of the kappa coefficient in the assessment and comparison of the accuracy of thematic maps obtained by image classification. *Remote Sens. Environ.* **2020**, *239*, 111630. [[CrossRef](#)]
71. Congalton, R.G. A review of assessing the accuracy of classifications of remotely sensed data. *Remote Sens. Environ.* **1991**, *37*, 35–46. [[CrossRef](#)]
72. Mathieu, L. Quantifying hydrothermal alteration: A review of methods. *Geosciences* **2018**, *8*, 245. [[CrossRef](#)]
73. Frutuoso, R.; Lima, A.; Teodoro, A.C. Application of remote sensing data in gold exploration: Targeting hydrothermal alteration using Landsat 8 imagery in northern Portugal. *Arab. J. Geosci.* **2021**, *14*, 1–18. [[CrossRef](#)]
74. Chattoraj, S.L.; Prasad, G.; Sharma, R.U.; van der Meer, F.D.; Guha, A.; Pour, A.B. Integration of remote sensing, gravity and geochemical data for exploration of Cu-mineralization in Alwar basin, Rajasthan, India. *IJAEO* **2020**, *91*, 102162. [[CrossRef](#)]
75. Pour, A.B.; Park, T.-Y.S.; Park, Y.; Hong, J.K.; Muslim, A.M.; Läufer, A.; Crispini, L.; Pradhan, B.; Zoheir, B.; Rahmani, O.; et al. Landsat-8, advanced spaceborne thermal emission and reflection radiometer, and WorldView-3 multispectral satellite imagery for prospecting copper-gold mineralization in the northeastern Inglefield Mobile Belt (IMB), northwest Greenland. *Remote Sens.* **2019**, *11*, 2430. [[CrossRef](#)]
76. Shirmard, H.; Farahbakhsh, E.; Pour, A.B.; Muslim, A.M.; Müller, R.D.; Chandra, R. Integration of Selective Dimensionality Reduction Techniques for Mineral Exploration Using ASTER Satellite Data. *Remote Sens.* **2020**, *12*, 1261. [[CrossRef](#)]
77. Sekandari, M.; Masoumi, I.; Pour, A.B.; Muslim, A.M.; Rahmani, O.; Hashim, M.; Zoheir, B.; Pradhan, B.; Misra, A.; Aminpour, S.M. Application of Landsat-8, Sentinel-2, ASTER and WorldView-3 Spectral Imagery for Exploration of Carbonate-Hosted Pb-Zn Deposits in the Central Iranian Terrane (CIT). *Remote Sens.* **2020**, *12*, 1239. [[CrossRef](#)]
78. Parsa, M.; Pour, A.B. A simulation-based framework for modulating the effects of subjectivity in greenfields' Mineral Prospectivity Mapping with geochemical and geological data. *J. Geochem. Explor.* **2021**, *229*, 106838. [[CrossRef](#)]
79. Bolouki, S.M.; Ramazi, H.R.; Maghsoudi, A.; Beiranvand Pour, A.; Sohrabi, G. A remote sensing-based application of bayesian networks for epithermal gold potential mapping in Ahar-Arasbaran area, NW Iran. *Remote Sens.* **2020**, *12*, 105. [[CrossRef](#)]
80. Parsa, M. A data augmentation approach to XGboost-based mineral potential mapping: An example of carbonate-hosted Zn-Pb mineral systems of Western Iran. *J. Geochem. Explor.* **2021**, *228*, 106811. [[CrossRef](#)]